

CONF-710601-5

RECEIVED BY DTIC JUN 18 1971

CONFIDENTIAL

TRANSMISSION ELECTRON MICROSCOPY OF RADIATION-INDUCED DEFECTS

Manfred R. Ruhle

Prepared for:

International Conference on Radiation-Induced Voids in
Metals, State University of New York, Albany, New York,
June 9-11, 1971

This report was prepared as an account of work sponsored by the United States Government. Neither the United States nor the United States Atomic Energy Commission, nor any of their employees, nor any of their contractors, subcontractors, or their employees, makes any warranty, express or implied, or assumes any legal liability or responsibility for the accuracy, completeness or usefulness of any information, apparatus, product or process disclosed, or represents that its use would not infringe privately owned rights.



U of C-AUA-USAEC

ARGONNE NATIONAL LABORATORY, ARGONNE, ILLINOIS

DISTRIBUTION OF THIS DOCUMENT IS UNLIMITED

189

TRANSMISSION ELECTRON MICROSCOPY OF RADIATION-INDUCED DEFECTS*

Manfred R. Rühle
Materials Science Division, Argonne National Laboratory
Argonne, Illinois 60439, U.S.A.

Abstract

Radiation-induced defect clusters of sizes larger than about 10 Å can be directly observed by means of transmission electron microscopy. The shape as well as the nature of the defects (vacancy or interstitial type) can be determined by comparing the results of the electron-microscopical contrast calculations for different possible defect clusters (Frank dislocation loops, perfect dislocation loops, voids, bubbles) with certain contrast experiments. The main emphasis in this paper will be put on the description of the results of contrast calculations for voids and bubbles. The influence of the focusing mode on the size and sign of the contrast figures is calculated. The results of the calculations are compared with some experimental observations of voids and bubbles in He⁺-bombarded gold films.

*This work was performed under the auspices of the U. S. Atomic Energy Commission.

TRANSMISSION ELECTRON MICROSCOPY OF RADIATION-INDUCED DEFECTS*

Manfred R. Rühle
Materials Science Division, Argonne National Laboratory
Argonne, Illinois, 60439, U.S.A.

I. INTRODUCTION

In recent years, transmission electron microscopy has become an extremely useful tool for the study of radiation damage in metals and reactor materials. Silcox and Hirsch¹ were the first who observed resolvable dislocation loops in neutron-irradiated copper. Later Makin and co-workers² found, in addition, a high density of small unresolvable defects ("black spots"). The density and size distribution of the radiation-induced defects were determined by counting, with the assumption that the diameters of the contrast figures correspond to the actual sizes of the defects. However, besides the density and size distribution of the defects, the nature and geometrical shape of the defects are of great interest. Especially, it is important to know whether the defects resulted from the agglomeration of vacancies or interstitials.

Considerable progress has been made in the theory of electron-microscopic contrast formation from defects in crystalline materials (see Hirsch et al.,³ Amelinckx et al.⁴). Aided by the theory, it is possible to calculate the contrast for any defect model with a known geometrical shape and a known strain field. To determine the nature of the defects in irradiated materials, first the contrast of various defect models has to be calculated. The results of the computations indicate differences in the contrast between different defect models. By exploiting these differences, it is possible to devise experiments by which the shape and the nature of the observable defects may be ascertained.

*This work was performed under the auspices of the U. S. Atomic Energy Commission.

These methods are briefly explained in Sections 2-5 in this paper. Emphasis is on the contrast of voids and bubbles. It will also be shown (Section 3) that this contrast can be influenced strongly by the focusing conditions of the objective lens.

In Section 6 some experiment details are summarized. Finally, in Section 7, experimental observations concerning the contrast of defects are described.

This paper emphasizes the methods for the analysis of radiation-induced defects. For a more detailed exposition of the theory of the contrast formation and a more complete review of the results on irradiated metals and reactor materials, the reader is referred to other articles (Rühle,⁵ Wilkens^{6,7}).

SHORT SUMMARY OF CONTRAST FORMATION IN TRANSMISSION ELECTRON MICROSCOPY

The contrast of lattice defects is formed by a diffraction contrast. As the electron beam passes through a crystalline solid, the beam is split into the direct beam and diffracted beams. (The directions of the diffraction beams depend on the lattice spacing through the Bragg equation.) If the direct beam is used for image formation (the diffracted beams are prevented from passing through the objective aperture), the so-called "bright field" is produced; if only one of the diffracted beams is used for image formation (i.e., the direct beam and all other diffracted beams are prevented from passing through the objective aperture), then a "dark field" image results. The variation of intensity observed on the micrograph depends on the local thickness of the foil, on the crystallographic direction of the incident beam, and on the focusing mode of the objective lens.

To obtain well-defined contrast conditions, the electron microscopic diffraction imaging should be performed under "two-beam diffraction conditions." Under these conditions, the orientation of the incoming electron beam with respect to the

the crystallographic axes is chosen so that the incident electron beam is reflected by one set of lattice planes only, i.e., besides the incident beam only one diffracted beam with diffraction vector g is strongly excited. However, since the Ewald sphere for electrons with energies of 100 keV or more is very flat, other reflections are always slightly excited. Especially, the "systematic reflections" (Bragg reflections with diffraction vectors ng , where (g = diffraction vector of the strong excited beam; $n = -1, \pm 2, \pm 3, \dots$) can never be avoided.

Under dynamical two-beam conditions, a "strong dark-field image" results by using the strong diffracted beam (diffraction vector g) for image formation. If one images the specimen with the diffraction vector $-g$ or $+2g$ ($n = -1, +2$), a "weak beam dark-field image" is produced.^{8,9} In the weak beam dark field more details on the defect structure are observable.

A critical length that is important for describing diffraction phenomena is the "extinction length" ξ_g . The value of ξ_g depends on the substance and on the particular reflecting plane. Small deviations $\Delta\theta$ of the direction of the incident beam from the exact Bragg conditions (Bragg angle θ) are described by the normalized excitation error $w = s \cdot \xi_g = \xi_g \cdot |g| \cdot \Delta\theta$. For $w \neq 0$, the effective extinction length ξ_g^w is given by^{3,10} $\xi_g^w = \xi_g / \sqrt{1+w^2}$. Micrographs taken under two-beam dynamical diffraction conditions (with $w \approx 0$) are called "dynamic images." Micrographs taken with a specific excitation error w are called "defined kinematic" images, those taken under unspecified kinematical diffraction conditions are called "undefined kinematic" images.

For calculations of the contrast of the disturbed lattice, "the column approximation" introduced by Hirsch, Howie, and Whelan¹¹ is applied. In this approximation it is assumed that, because of the smallness of the diffraction angle 2θ of the electrons, the intensity at a given point on the micrograph is

determined entirely by the varying diffraction conditions. This approximation has been justified by comparing the results of the column approximation with those of the exact solution of the problem¹²⁻¹⁴ for the case where the defects are imaged with a strong excited beam. However, in the case of weak diffracted beams, this approximation is applicable only in specific cases.¹⁵

If the lattice planes in the neighborhood of the defects are bent, the contrast can be calculated by solving the differential equations of dynamical two-beam approximation numerically. In such computations, the quantity characterizing specific defects is the z -derivative of the displacement field of the defect, where z denotes the directions of the bisector of the incident and the reflected electron beams (two-beam case).

There are several physical equivalent formulations of these differential equations. The scattering by the defects may be described in terms of plane waves,¹⁰ Bloch waves,^{16,17} or modified Bloch waves.¹⁸ For numerical integrations, Bloch wave equations are preferable because a scattering between the Bloch waves takes place only where the z -derivation of the displacement field is essentially different from zero. Therefore the Bloch wave equations must be solved only in the regions close to the defect.

For small defect clusters (small compared with the effective extinction length of the operating diffraction vector), the tails of the contrast profile can be calculated analytically in a first-order Born approximation.^{7,18} From these approximations, general features of the contrast figures (i.e., symmetry relations and direction of contrast) can be obtained. The first-order Born approximation is especially helpful to determine the expected contrast of perfect dislocation loops that are under different orientations with respect to the incident electron beam.⁷

A very important parameter in all contrast calculations is the parameter of the anomalous absorption,¹⁰ which is assumed to be ≈ 0.1 or slightly below this value.^{19,20}

B. DIFFRACTION CONTRAST FROM BUBBLES (WITHOUT STRAIN FIELD)

Both atomic defects (vacancies and interstitials) and clusters of these atomic defects are nucleated in irradiated materials. Only the clusters of agglomerates that are larger than at least the resolution of the electron microscope can be observed by means of transmission electron microscopy. The observable agglomerates will be simply called defects. There are essentially two different types of defects: defects with or without a strain field in the vicinity of the defects.

In this Section the contrast of defects without a strain field in the vicinity of the defects will be discussed, and in Section 4 the contrast of defects with a strain field will be described.

3.1. "In-focus" Contrast of Defects without Surrounding Strain

For the contrast calculations of defects without surrounding strain, it is assumed that the vicinity of the void has the structure of the ideal crystal. For simplicity, a void not surrounded by a strain field will be called a bubble. This case is important for small gas-filled voids or large partially or empty voids, since in the latter case the expected strain is negligible.*

* At this point it should be noted that, in the case of a gas-filled bubble in equilibrium with the surrounding matrix, strain will be left in the matrix. Under the conditions of thermal equilibrium, the gas pressure is $p = 2\sigma/r_0$, where σ is the surface tension of the solid and r_0 is the radius of the bubble. Shuttleworth,²¹ Herring,²² and Lidiard et al.²³ pointed out that the surface energy γ and the

surface tension σ are not necessarily equal for solids. (By surface energy we mean those terms in the free energy of a solid that are proportional to the surface area.) These two quantities are related by

$$\sigma = \gamma + F \cdot \frac{d\gamma}{dF},$$

where the differentiation indicates a change of the area F of the bubble under conditions in which the number of surface atoms remains constant. The surface tension σ can be considerably different from the surface energy in the case of copper; σ has a value that ranges between $-0.2\gamma \lesssim \sigma \lesssim 0.3\gamma$ ²⁴

The contrast of bubbles was calculated by Ashby and Brown²⁵ and in detail by Van Landuyt et al.;²⁶ the results of Van Landuyt et al. were applied by Ingram²⁷ and Ruedt.^{28,29} The contrast of the bubbles can best be calculated by the matrix method developed by Gevers³⁰ and Amelinckx.³¹

With this method the amplitudes of the transmitted beam T_{z_1} and of the scattered beam S_{z_1} are calculated at the lower surface of a perfect crystal (thickness z_1) by multiplying the amplitudes of the incoming beams (T_0, S_0) with the "scattering matrix" $M(z_1)$.^{30,31} If a perfect crystal (thickness t) contains a bubble of thickness z_2 , the amplitudes T^b and S^b of the transmitted and reflected beam at the exit surface are (see Fig. 1):

$$\begin{pmatrix} T^b(x,y) \\ S^b(x,y) \end{pmatrix} = M(z_3; x,y) V(z_2; x,y) M(z_1; x,y) \begin{pmatrix} 1 \\ 0 \end{pmatrix}. \quad (1)$$

The amplitudes T^b and S^b are in general a function of the coordinates (x,y) , since the thickness z_2 of the bubble with an arbitrary shape depends on (x,y) . We restrict ourselves mainly to the case where the z_2 dimension of the cavity is constant, see Fig. 1. Clearly, a bubble of arbitrary shape can always be

decomposed in a sequence of bubbles with constant thickness. The variation over the projected area of the bubble can easily be obtained by using the thickness-intensity relations that are described here. Contrast of bubbles with a spherical shape will be discussed later in some detail.

In Eq. (1) the scattering matrix $M(z_1)$ can be described as [the dependence of z_2 on the (x,y)-coordinates is not noted explicitly any more]:

$$M(z_1) = M_1 = \begin{pmatrix} T_1 & S_1^- \\ S_1 & T_1^- \end{pmatrix}, \quad (2)$$

where the explicit expressions for T_1 and S_1 are in good approximation:^{26,30}

$$T_1 = \cos \pi \alpha z_1 - i s \xi_g^w \sin \pi \alpha z_1$$

$$S_1 = \frac{i}{\sqrt{1+w^2}} \sin \pi \alpha z_1,$$

with

$$\alpha = \frac{1}{\xi_g^w} + i \frac{1}{\tau_g \sqrt{1+w^2}}, \quad w = s \xi_g \quad \text{and} \quad \xi_g^w = \frac{\xi_g}{\sqrt{1+w^2}},$$

where s is the excitation error, t_g is the extinction length for the diffraction vector g , and τ_g is the corresponding absorption length.

$V(z)$ in Eq. (1) is the "vacuum matrix."

$$V(z_2) = e^{-2\pi i \epsilon \Delta z} \begin{pmatrix} 1 & 0 \\ 0 & e^{2\pi i s_1 z_2} \end{pmatrix}. \quad (3)$$

In Eq.(3), the factor $e^{-2\pi i \epsilon \Delta z}$ describes the phase difference between a beam passing through a bubble of thickness Δz and a beam passing through the regions of the perfect crystal.

This phase shift is caused by the difference of the mean inner potential V_0 in the gas-filled bubble and the perfect crystal. From the mean inner potential V_0 (< 0) in a metal, the refraction index ϵ_0 can be calculated to

$$\epsilon_0 = - \frac{eV_0}{2E} k_0 \quad (4)$$

where e is the charge of an electron, E the total energy of the electron, and k_0 the vacuum wave vector of the electrons.

The phase factor can be neglected if one images the bubbles "in-focus," i.e., if one images (with the objective lens) exactly the exit surface of the foil. However, if one images the defect "out-of-focus" (i.e., if one images a plane with a distance from the exit surface), the phase factor is very important, see Section 3.2.

The column vector $\begin{pmatrix} 1 \\ 0 \end{pmatrix}$ in Eq. (1) represents the initial values of T and S at the entrance surface ($z = 0$), the matrix M_1 describes transmission through the first portion of the crystal with thickness z_1 , and the matrix $V(z_2)$ determines the scattering by the bubble (thickness z_2). The value of the excitation error s to be used in $V(z_2)$ is that of the preceding perfect column, therefore s is constant since the crystal is perfect apart from the void. M_3 describes the scattering through the second part of the perfect crystal with thickness z_3 .

From the amplitudes T^b and S^b the intensities can be calculated; however, normal absorption also has to be taken into account in the present case, i.e., the intensities have to be multiplied by an absorption factor

$$e^{-\mu(z_1 + z_2)},$$

where μ is the normal absorption coefficient, and absorption by the bubble is obviously neglected.

On the other hand, the amplitudes T^P and S^P in the perfect regions of the crystal can be calculated to

$$\begin{pmatrix} T^P \\ S^P \end{pmatrix} = M(t) \begin{pmatrix} 1 \\ 0 \end{pmatrix}, \quad (5)$$

where t is the thickness of the film. In this case an absorption factor $e^{-\mu t}$

has to be taken into account for the intensities I . The contrast is defined by

$$C_{T,S} = \frac{I_{T,S}^b - I_{T,S}^P}{I_{T,S}^P},$$

(the subscripts T and S indicate the intensity of the transmitted or scattered beam).

As one can note from Eqs. (1), (2), and (3), the contrast depends on the thickness t of the film, the thickness z_2 of the bubble (which may vary over the cross section of the void), the normal absorption factor μ and the anomalous absorption factor τ_g , and on the excitation error w .

In our considerations we restrict ourselves on the case $s = 0$, i.e., the exact Bragg condition. In the dynamical condition ($s = 0$), the calculated contrast of the bubble is independent of the depth-position z_2 of the defect, since Eq. (1) simplifies to

$$\begin{pmatrix} T^b \\ S^b \end{pmatrix} = e^{-2\pi i \epsilon_0 \Delta z} \cdot M_3 M_1 \begin{pmatrix} 1 \\ 0 \end{pmatrix}. \quad (6)$$

Since the basic property of the M matrices is that

$$M(z_1) \cdot M(z_1) = M_3 \cdot M_1 = M(z_1 + z_3) \text{ (see Ref. 30),}$$

the relation in Eq. (6) describes transmission and scattering by a perfect crystal of thickness $(z_1 + z_3)$. The intensity of an electron beam passing through the bubble

can be calculated by

$$I_{T,S}^b = I_{T,S}^p (z_1 + z_3),$$

and the contrast of the bubbles is

$$C_{T,S} = \frac{I_{T,S}^p (z_1 + z_3)}{I_{T,S}^p (t)} - 1. \quad (7)$$

The thickness-intensity relationships for bright field and dark field are plotted in Fig. 2 for different factors of normal absorption μ . For different materials and different operating reflection vectors, different experimentally determined values of μ have to be applied. The curves for bright field plotted in Fig. 2 include the upper and lower values for different materials imaged with diffraction vectors of not too high order.

From the curves plotted in Fig. 2, the theoretical predicted contrast of voids in bright field and dark field can be calculated from Eq. (7). The expected contrast of small bubbles with constant thickness is plotted against the foil thickness in Fig. 3. It follows that the bubbles exhibit the strongest contrast in a very thin region of the crystal; the thickness of the crystal should be smaller than about three extinction lengths. The contrast depends sensitively on the exact value of the foil thickness, especially in the case of a very thin crystal region. The contrast is strongest at thicknesses slightly smaller or larger than 0.5 extinction lengths, i.e., at the front or the rear of the first dark thickness fringe in dark-field images or at the front of the second dark fringe in bright-field images. These results have been verified experimentally by Ruedl.^{28,29}

The calculated contrast figures of bubbles with different (constant) thicknesses z_2 are plotted for a constant foil thickness (four extinction distances)

in Fig. 4. The curves indicate that for small (normal) absorption factors μ the bubbles exhibit predominantly negative contrast in bright field and predominantly positive contrast in dark field. Figure 4 also indicates that the sign of the contrast can be different for bubbles with different thicknesses z_2 .

So far we calculated the electron-microscopical contrast for bubbles with a constant thickness z_2 . If the thickness of the bubble varies over the projected area of the bubble, the sign and magnitude of the contrast will also vary over the projected area. For dynamical two-beam imaging conditions ($w = 0$), the contrast can easily be obtained from Fig. 2 for each bubble thickness.

We calculated the "in-focus" contrast for bubbles with a spherical shape. For these bubbles the thickness z_2 (compare with Fig. 1) depends only on the distance r from the center of the bubble:

$$z_2 = 2 R_b \sqrt{1 - \rho^2},$$

where R_b is the radius of the bubble and ρ the reduced distance from the center of the bubble $\rho = \frac{r}{R_b}$ ($0 \leq \rho \leq 1$). The dependence of the sign and magnitude of the contrast as a function of the distance ρ can be determined with Fig. 2 for bubbles with different radii R_b in foils of different thicknesses t .

The sign of the contrast ("bright" or "dark" compared to the background intensity) produced by bubbles with diameters smaller than $0.5 \xi_g$ extinction distances ξ_g depends on the thickness of the foil; however, it will always be the same over the whole range of ρ . For bubbles with diameters between $0.5 \xi_g$ and $1.0 \xi_g$ the sign of the contrast can change over the projected range of the bubble ($0 \leq \rho \leq 1$), if the foil thickness is about $(n + 1/4) \xi_g$ ($n = 3, 4, 5, \dots$). If the diameter of the spherical bubble is larger than ξ_g , the sign of the contrast changes at least once over the range of ρ .

Obviously, the magnitude of the contrast depends on the distance ρ for all spherical bubbles of different sizes. The contrast profiles for two examples ($R_b = 0.1 \xi_g$ and $R_b = 0.4 \xi_g$) are plotted in Fig. 5 as a function of $\rho = r/R_b$. The foil thickness is $3.75 \xi_g$. In both cases, maximum contrast is obtained for $\rho = 0$. The small bubble ($R_b = 0.1 \xi_g$) reveals for $t = 3.75 \xi_g$ a negative contrast; the intensity inside the projected area of the bubble (onto the image plane) is always smaller than the background intensity. As expected, the sign of the contrast does not change over the whole range of ρ ; however, the magnitude of the contrast decreases with increasing ρ . This contrast will be barely visible, especially since the weak contrast changes slowly over the radius of the small bubble. For the large bubble ($R_b = 0.4 \xi_g$) the calculated contrast is a bright spot surrounded by a dark ring, i.e., the sign of the contrast changes in this case. The diameter of the bright part is 0.87 of the diameter of the bubble, the outer diameter of the dark ring corresponds to the actual diameter of the bubble.

For other bubble diameters and foil thicknesses, similar or more complicated contrast figures can be calculated. However, for all in-focus contrast calculations, the outer diameter of the contrast figures corresponds always best to the actual size of the bubbles.

For $w \neq 0$, the in-focus contrast of large bubbles ($d \geq 0.3 \xi_g^w$) may be brighter or darker than the background intensity, depending on the depth position of the bubble and on the magnitude and sign of w (see Ref. 26). The contrast of small bubbles is so weak that it is not possible to observe the defect for large w .

3.2 "Out-of-focus" Contrast of Bubbles

We derived formulas in Section 3.1 that can be used to calculate the amplitudes of the transmitted and scattered wave field at each point of the exit surface of the foil. The intensity distribution can be imaged with the electron microscope by imaging the exit surface of the foil, i.e., the lower plane of the foil coincides with the image plane of the objective lens. In this way an "in-focus" picture is produced.

However, if one images, as sketched in Fig. 6, a plane that has a certain distance ζ_i from the lower surface of the foil, one produces an "out-of-focus" picture. The intensity distribution of an "out-of-focus" picture will be, in general, different from the "in-focus" picture, since the waves of the wave field at $\zeta = 0$ (exit surface of the foil) interfere with each other before reaching the image plane at $\zeta_i \neq 0$.

The wave field in the image plane (at a distance ζ_i from the foil, see Fig. 6) must be calculated from the wave field at $\zeta = 0$. The coordinate system will be chosen as shown in Fig. 6. We normalize the wave field at $\zeta = 0$ outside the bubble so that $\psi(r, 0) = 1$ [$r = r(\xi, \eta)$]. Then we can express the wave field for $r < r_0$ as $\psi(r, 0) = 1 + \Delta(\xi, \eta)$, where $\Delta(\xi, \eta)$ is a complex quantity.

The two-dimensional Fourier transformation of the wave field at $\zeta = 0$ is

$$\tilde{\psi}(p) = \int_0^{\infty} \psi(r) \exp(-2\pi i p \cdot r) d^2r, \quad (8)$$

with $p = p(p_\xi, p_\eta)$.

The amplitude of the wave field at the point $(\xi, \eta) = r$ at a distance ζ from the exit surface is then given by (for details see Ref. 32)

$$\psi(\underline{r}, \zeta) = \int_0^{\infty} \tilde{\psi}(p) \exp \left[2\pi i (p \cdot r + \zeta \sqrt{k_0^2 - p^2}) \right] d^2p. \quad (9)$$

This equation satisfies the necessary conditions that the wave vector of the electrons is k_0 and Eq. (9) with $\zeta = 0$ leads to Eq. (8).*

* Equation (9) also can be obtained by solving the Kirchoff integral of the diffraction theory.^{33,34} It should be noted that the influence of the astigmatism of the objective lens and the finite aperture on the "out-of-focus" image can be neglected for defect structures larger than about 8 \AA .³⁴

Since $p^2 \ll k_0^2$ we develop $\sqrt{k_0^2 - p^2} \approx k_0 - \frac{1}{2} \frac{p^2}{k_0}$, (10)

and obtain

$$\psi(\underline{r}, \zeta) = \exp(2\pi i k_0 \cdot \zeta) \int_0^{\infty} \tilde{\psi}(p) \exp \left[2\pi i \left(\underline{p} \cdot \underline{r} - \frac{1}{2} \frac{p^2}{k_0} \zeta \right) \right] d^2p, \quad (11)$$

where the phase factor $\exp(2\pi i k_0 \cdot \zeta)$ can from now on be omitted.

We calculate the "out-of-focus" contrast for a bubble, and we restrict ourselves on cases where the projection of the bubble onto the (ξ, η) plane is a circle with radius r_0 . Furthermore, we assume that $\Delta(\xi, \eta)$ depends only on the distance from the center of the bubble and not on the azimuth angle φ .

With Eq. (8), we obtain from Eq. (11)

$$\psi(\underline{r}, \zeta) = \int_{p=0}^{\infty} \int_{r'=0}^{r'=r_0} \psi(r') \cdot \exp \left[2\pi i \left((\underline{p}, \underline{r}-\underline{r}') - \frac{1}{2} \frac{p^2}{k_0} \cdot \zeta \right) \right] d^2p d^2r. \quad (12)$$

The integration over d^2p can be solved analytically. If we introduce a polar coordinate system (r, φ) , the integration over the azimuth angle φ can also be

performed analytically when $\psi(r') = 1 + \Delta(|r|)$, and we obtain

$$\psi(r, \zeta) = 1 - 2i\beta \exp [i\beta\rho^2] \int_{\rho'=0}^1 \Delta(\rho') J_0(|2\beta\rho\rho'|) \exp [i\beta\rho'^2] \rho' d\rho', \quad (13)$$

with $\beta = \frac{\pi k_o r_o^2}{\zeta}$, $\rho = \frac{|r|}{r_o}$ and J_0 the zero-order Bessel function. Explicit calculations of $\psi(r, \zeta)$ require that $\psi(\rho') = 1 + \Delta(\rho')$ is known. $\psi(\rho')$ is essentially different for bubbles of various sizes and shapes, it can be calculated from Eqs. (1) and (5).

3.2.1 Small Bubbles. If the dimensions of the bubble are very small compared to the operation extinction length, $\Delta(\rho')$ will be proportional to the actual thickness z_2 of the bubble at the distance $\rho = \frac{r'}{r_o}$.* In this case is

* This approximation is valid for spherical bubbles with a diameter smaller than $0.25 \xi_g^{.32, 34}$

$$\psi(\rho') = 1 + \delta G(\rho') . \quad (14)$$

In Eq. (14), δ describes the change of $\psi(\rho')$ in the center of the bubble. The quantity δ is complex and can be calculated from Eqs. (1) and (5). For small bubbles, the imaginary portion of δ is most significant, i.e., the phase shift of the wave going through the center of the bubble relative to the wave field in the perfect crystals. From Eq. (3) the phase factor will be

$$e^{-2\pi i \epsilon_o \Delta z} - 1 \approx -2\pi i \epsilon_o \Delta z$$

where Δz is the thickness of the bubble at $\rho = 0$.

The term $G(\rho)$ in Eq. (14) is a geometrical factor that describes the thickness of the bubble as a function of the distance $\rho = \frac{r}{r_0}$ from the center of the bubble. For spheres, G is $G = \sqrt{1 - \rho^2}$, and for small disks, G is $G = 1$.

For these two simple geometrical shapes, the intensity distribution was calculated with a computer from Eq. (13). For the integration it was assumed that the mean inner potential is -10 V .³

Some results of the calculations are represented in Figs. 7(a) and 7(b). The reduced intensity I/I_0 ($I_0 =$ background intensity) of the "out-of-focus" contrast is plotted as a function of the distance $\rho = \frac{r}{r_0}$ from the bubble center at $r = 0$.

As pointed out in Section 3.1, the contrast of small bubbles (radius $r \leq 0.1\xi_g$) is weak for "in-focus" conditions and large foil thicknesses. The small bubbles are nearly invisible. Figures 7(a) and 7(b) indicate that the small defects reveal a stronger contrast if they are imaged under "out-of-focus" conditions.*

*It should be noted that for the contrast calculations the mean inner potential of -10 V was assumed. Actually, this value is too low for almost all metals; a value of -20 V should be closer to the real value of V_0 . Preliminary calculations have shown that for $V_0 = -20 \text{ V}$ the absolute values of the contrast are increased, but the shape of the contrast profiles are unchanged. Especially, the ρ -value, for which $I/I_0 = 1$ (no contrast) remains within 2% even when V_0 is changed from -10 V to -20 V .

The calculated contrast is, for negative values of ζ , a bright, circular center surrounded by a sequence of dark and bright Fresnel fringes. However, only the contrast of the first dark Fresnel fring is strong enough to be visible.

The size of the white center represents, within 10%, the real diameter of the bubble for $\zeta \leq -1$. However, the diameter of the white center exceeds the actual bubble size for $\zeta > 1$. This is true for small spherical bubbles and for small disks.

The calculated ratios of the inner and outer diameters of the first dark Fresnel fringe to the actual bubble diameters are plotted in Fig. 8 as a function of the actual bubble diameter for $\zeta = -8000 \text{ \AA}$. Figure 8 indicates that, only for bubbles smaller than 20 \AA , the diameter of the inner bright area (equivalent to the inner diameter of the first dark Fresnel fringe) deviates more than 10% from the actual bubble diameter.

However, the results represented in Fig. 8 clearly show that the outer diameter of the first dark Fresnel fringe is much larger than the actual size of the bubble. Therefore, this quantity should never be used to determine the size of small bubbles.

If one calculates the out-of-focus intensities for $\zeta > 0$, the contrast is reversed; a dark spot is surrounded by a series of bright and dark rings.

3.2.2. Large Bubbles. For large bubbles (diameter larger than 0.25 extinction length) the wave field at $\zeta = 0$ must be calculated according to Eqs. (1) and (5). With the numerically obtained wave field, Eq. (13) has to be integrated. The integration was performed only for a few bubble sizes, and one result is plotted in Fig. 9. The "out-of-focus" contrast was calculated for a bubble with a radius of $0.4\xi_g$, and the thickness of the film was $3.75\xi_g$. The "in-focus" contrast calculations (compare Fig. 5 and the heavy solid line in Fig. 9) predict a bright circular center surrounded by a dark ring.

For a defocusing distance $\zeta = -6000 \text{ \AA}$, the contrast is modified when compared with the "in-focus" contrast. However, the general feature of the contrast remains the same since the small intensity oscillations for $\rho < 0.8$ cannot be observed experimentally. For $\zeta = -6000 \text{ \AA}$, the outer diameter of the first dark ring corresponds to the actual diameter of the bubble. This result is not correct for $\zeta = +6000 \text{ \AA}$ because in this case, the outer diameter of the first intensive dark ring is at $\rho = 1.15$. The results of Fig. 9 can be understood in terms of the Fresnel diffraction theory.³²

Some preliminary calculations for additional bubble diameters show that the results from Fig. 9 cannot be generalized for all sizes of bubbles and foil thicknesses. Detailed results of contrast calculations will be published elsewhere.³²

4. CONTRAST OF SMALL DEFECTS WITH SURROUNDING STRAIN FIELD

The lattice planes are bent in the vicinity of a defect if the defect possesses a strain field. Therefore, a scattering between the wave fields existing in the lattice occurs, which changes the amplitudes at points close to the defect.

If the defects are smaller than the extinction lengths, their structure and shape are not directly resolvable on micrographs. However, as shown in different papers (for a summary see Refs. 4-6.), information on the type and shape of the defects can be obtained by imaging the defects under well-defined dynamic and kinematic diffraction conditions. The results of the observations have to be compared with the results of contrast calculations, which will be described shortly.

Defects produced by condensation of vacancies and interstitials are distinguished by the sign of the elastic displacement in the vicinity of the defects;

defects produced by interstitials have a positive sign (positive misfit parameter³⁵); defects produced by condensation of vacancies have a negative sign (negative misfit parameter).

For dynamic and defined kinematic diffraction conditions, the results of the contrast calculations are available for several defect models, such as Frank dislocation loops, perfect dislocation loops, and strain centers with a spherically symmetrical displacement field.^{5,6,36-39} The important features of the contrast are summarized in Section 4.1, additional details on the contrast for voids are represented in Section 4.2, and in Section 4.3, the required experiments for the analysis of the defects are described.

4.1. Results of Contrast Calculations for Small Defect Clusters

A. Under two-beam dynamic diffraction conditions, a small defect within a surface layer of about one extinction distance ξ_g^w thickness shows a black-white (BW) contrast (see Figs. 10, and 11). A BW contrast is described by a vector ℓ pointing from the center of the black portion to the center of the white portion.

The magnitudes of the black and white portions of the contrast (BW contrast) strongly depend on the exact value of the foil thickness, if the foil is thinner than four extinction distances. Highest contrast is expected from a defect in bright field in foils with a thickness of $t_1 = (2n + 1) \xi_g^w / 2$ ($n = 0, 1, 2, \dots$) and in dark field in foils with a thickness $t_2 = n \xi_g^w$ ($n = 1, 2, 3, \dots$). The defects are nearly invisible in bright field in foils with a thickness of t_2 and in dark field in foils with a thickness of t_1 .

The magnitude of the BW contrast is independent of the exact value of the foil thickness t , if t is larger than ~ 5 extinction lengths. In this case the thick foil approximation is applicable.¹⁸

B. The BW contrast of small defects shows the following characteristic features for different shapes of defects:

(1) For small dislocation loops, the direction ℓ of the BW contrast is determined by the main component of $d(g \cdot R)/dz$ where g is the diffraction vector, $R(x,y,z)$ is the displacement field of the defect, and z is the coordinate parallel to the reflecting lattice planes. For defects with an isotropic displacement field (voids, see Section 4.2), ℓ is always parallel to $+g$ or $-g$, independent of the direction of the fraction vector.

For Frank dislocation loops (the Burgers vector b of the loop is perpendicular on the loop plane), ℓ is parallel or antiparallel to b independent of the diffraction vector with which the defects are imaged. However, the angle between b and the diffraction vector must be smaller than $\sim 60^\circ$.

For perfect loops (Burgers vector is not perpendicular on the loop plane), the direction of the BW contrast ℓ is, in general, no longer parallel or antiparallel to Burgers vector b ; the angle between ℓ and b depends on the loop orientation relative to the diffraction vector g .³⁶⁻³⁸ For certain orientations, complex contrast figures are calculated.^{36, 37, 39}

(2) The sign of $(g \cdot \ell)$ depends on the sign of the defect (vacancy or interstitial) as well as on the distance of the defect to the nearest foil surface. Thus for a defect with a given sign of the

misfit parameter, the sign of $(g \cdot \ell)$ oscillates, as shown in Fig. 11, with the depth position of the defect inside the foil (depth oscillations). If a defect lies close to a boundary of the layers (transition regions), complex contrast figures are calculated for all shapes of defects.³⁶

C. Contrast calculations show that the defects appear as black dots under both unspecified (many-beam) and defined kinematic diffraction conditions. As shown by Maher et al.,³⁹ the contrast width under defined kinematic conditions also depends on the diffraction vector g . Preliminary many-beam calculations when compared with experimental observations,⁴⁰ have shown that the diameter of the contrast figures (at 10% deviation from the background intensity) corresponds best to the actual size of the defect if the foil orientation relative to the electron beam is close to a $\langle 100 \rangle$ or a $\langle 110 \rangle$ orientation.

The largest diameter of the black dots (which, in general, do not have a circular shape) on positive prints corresponds to the diameter of the defect.

4.2. Results of Contrast Calculations for Voids

The contrast of voids with a surrounding strain field has been calculated for different void sizes, different amounts of strain in the vicinity of a void, different diffraction conditions, and different foil thicknesses. In this calculation, both contrast effects, i.e., diffraction contrast by the empty space inside the foil (see Section 3) and by the strain, were considered. So far, only "in-focus" contrast has been calculated for voids with a strain field.

The contrast due to the strain in the vicinity of the void is strongest under exact two-beam diffraction conditions. The strain is described by means of the (dimensionless) "normalized" misfit parameter

$$P = \Delta V \cdot \frac{g}{\pi \xi_g^w},$$

where ΔV represents the volume misfit of the defect, with

$\Delta V = \epsilon_m \cdot \frac{4\pi}{3} R_s^3$ for a spherical void ($R_s =$ radius of the inclusion); ϵ_m is the relative volume misfit, which is for a partially gas-filled void⁴²

$$\epsilon_m = \frac{2\gamma p R_s}{4\mu R_s},$$

where p is the pressure inside the void, γ is the surface energy (see Section 3.1) and μ is the shear modulus. Figure 12 shows the results of the calculations concerning the visibility and type of contrast.⁴³ The diagram is divided into three areas. In area A (small defects, large misfit parameter) BW contrasts with depth oscillations (Fig. 11) are expected. In area B, the BW contrasts are calculated; however, the depth oscillations of the BW contrasts are suppressed, since the boundary conditions at the foil surfaces are changed. The direction ℓ for all BW contrasts of defects belonging to area B is the same as for small defects lying in the first layer L_1 as described in Fig. 10 ("Ashby-Brown case"⁴⁴). Defects in area C (large voids) reveal no BW-contrast, with or without depth oscillations. The contrast of the large voids is determined mainly by the thickness contrast described in Section 3.

For small voids (area A) the absolute value of the strain can be estimated by comparing the results of the calculations with quantitatively evaluated micrographs. It should be possible to determine at least the order of magnitude of strain around the small voids by imaging the defects with different diffraction vectors g . The value of the normalized

misfit parameter P is changed by these experiments.

A comparison of the experimental observations with the contrast calculations will give the value of ϵ_m . However, the quantitative value of the contrasts depends on the exact value of the foil thickness t , if t is smaller than 4 extinction distances. It must be noted that if the diffraction vector g is changed the reduced foil thickness (in extinction distances) is changed. Therefore, the quantitative evaluation is possible only for thick foils.

4.3. Required Experiments for the Analysis of Small Defects

- A. The Burgers vector and the shape of small defects can be determined by imaging the defects under different two-beam diffraction conditions, i.e., with different g vectors. The defects reveal BW contrasts. From the directionality of the BW contrasts, the most simple geometrical shape can be determined.
- B. The type of small defects (vacancy or interstitial) can be determined by measuring the distance between the depth position and the nearest foil surface with the stereo technique^{45,46} and by comparing the results of the measurement with the calculated depth-oscillations (Fig. 11).
- C. The volume density and size distribution of the defects can be evaluated from micrographs taken under kinematic diffraction conditions. The thickness of the film has to be determined by stereo measurements.^{5,6}

5. CONTRAST FROM LARGE DISLOCATION LOOPS

If the diameter of a dislocation loop is larger than about one extinction distance, the geometrical shape of the loop is resolvable with the electron microscope. The contrast of the large loop can be explained by the contrast of a single dislocation line.

5.1. Contrast of a Perfect Dislocation Loop

A perfect dislocation loop consists of a closed dislocation line; no stacking fault is present inside the loop. The Burgers vector of the dislocation line can be determined with the rule $(g \cdot b) = 0$ for (nearly) vanishing contrast.

From contrast calculations by Howie and Whelan,¹⁰ for a single dislocation, it is known that in the defined kinematic case ($w \geq 1$) the actual position of the dislocation does not coincide with the black line (minimum of the contrast profile). The black line will always be on the side of the dislocation where the lattice bending (caused by the dislocation) locally reduces the excitation error w ; the magnitude of the shift depends on the magnitude of w .^{*} With this property of the dislocation contrast, one can determine

*

For $w \approx 0$ the minimum of the contrast profile coincides with the position of the dislocation line.

the type of the loop.⁴⁷⁻⁵⁰

The analysis can only be applied for loops that have a Burgers vector 'b' perpendicular on the loop plane. The loop plane has to be inclined to the image plane (the image plane is the plane perpendicular to the incident electron beam). For cases where the loop planes are parallel or perpendicular to the image plane, the observable shapes of the loops vary insensitively with the tilting of the specimen. If the loop is inclined, the portions of the loop most strongly inclined to the image plane give rise to a weaker contrast with the

other portions of the loop.*

* The line through the two weak parts is parallel to the trace of the image plane and the habit plane.

The loop normal n may be defined so that the angle between n and the direction of the incident electron beam k_0 is always acute. Then we may differentiate between two-loop plane orientations (i) $(g \cdot n) > 0$ and (ii) $(g \cdot n) < 0$. A tilting experiment (tilt axis perpendicular to g) with high tilting angles and by observing the change of the projected loop width will determine which of the two orientations occurs for a specific loop.

From the above-mentioned fundamental property of the dislocation contrast, it follows for $w \neq 0$ that the contrast lies either outside [case (a)] or inside [case (b)] the projected loop position. A decision between the two possibilities may be reached either by changing the sign of w^{h7} near the same diffraction vector g , or by changing from g to $-g$ with the fixed sign of w .** The latter experiment is normally preferred since,

** Effectively one has to change the sign of $(g \cdot b)_s$.

especially in thick films, the transmissivity is low for negative values of w .

If all experiments were performed with $w > 0$, one determines the nature of the loop by combining the results of large-angle tilting experiments (case i and case ii) with the results of the $+g/-g$ experiments.

The following rules are valid for differentiation between vacancy and interstitial loops:

(i) + (a) or (ii) + (b) \rightarrow vacancy loop

(i) + (b) or (ii) + (a) \rightarrow interstitial loop.

This rule works correctly only if Burgers vector b is perpendicular to the loop habit plane. The above rules are no longer valid if b contains a shear component b_s , and if b_s changes the sign of $(g \cdot b)$ relative to the corresponding sign of $(g \cdot b_e)$.^{*} This occurs for certain orientations

* b_e is the component of the Burgers vector that is perpendicular to the loop plane.

of b_s relative to g and for certain magnitudes of b_s . To determine the nature of the loops, the direction of Burgers vector is also needed, and this direction can be evaluated by a sequence of different tilting experiments (Maher and Eyre^{51,52}).

5.2 Contrast of a Dislocation Loop with Stacking Fault (Partial Dislocation)

If a dislocation loop contains a stacking fault, the surrounding dislocation is, in general, a partial dislocation. In this case $(g \cdot b)$ will not be an integer. Extended contrast calculations by Silcock and Tunstall⁵³ have shown that the contrast of the dislocation is much weaker for $(g \cdot b) = -\frac{2}{3}$ than for $(g \cdot b) = +\frac{2}{3}$ (in both cases $w \approx 1$). Based on this result and on a similar method described in Section 5.1, it is possible to determine the nature of the loops. The fault displacement vector R can be determined with the rule $g \cdot R = 0$, i.e., the stacking fault is invisible if R is perpendicular to g .

6. SOME EXPERIMENTAL DETAILS

6.1 Determination of the Excitation Errors

The sign and magnitude of the excitation error w may be determined from the Kikuchi line pattern (see Hirsch et al.³). These lines usually can be observed in fairly thick crystals; however, the number of defects inside the crystal should not be too great. Kikuchi lines are due to Bragg reflections of inelastically scattered electrons, which are "incident" under all possible angles. The geometric locus of the Bragg reflected beams is a wide cone with an opening angle of $90^\circ - \theta$ ($\theta \approx$ Bragg angle). This cone intersects the photographic plate along parts of a hyperbola, which becomes very nearly a straight line because of the large opening angle and the large distance between the specimen and the plate. Two parallel Kikuchi lines always belong to one set of lattice planes, the distance f between the lines corresponds to an angle difference 2θ , which is also the distance of the corresponding diffraction spots of the operating diffraction vector.

Under dynamic two-beam conditions, the Kikuchi line-pair passes through the spots of the incident and diffracted beams. If the foil is now rotated over a small angle $\Delta\theta$, the positions of the diffraction spots are (nearly) unchanged, whereas the beam producing the Kikuchi lines rotates over the same angle. Therefore, the Kikuchi lines are displaced with respect to the diffraction spots over the distance

$$\Delta f = f/2\theta \cdot \Delta\theta$$

From this $w = \xi_g \cdot s = \xi_g \cdot g \cdot \Delta\theta$ can be determined. The sign of w is defined such that w is negative if the displacement of the Kikuchi lines on the diffraction pattern is toward the spot of the direct beam and is positive if the displacement is away from the spot of the direct beam.

6.2. Determination of Foil Orientation and Tilting Angle in Stereo Measurements

For certain experiments, the exact orientation of the foil relative to the incident electron beam must be known. As shown by Thomas⁵⁵ and co-workers, the orientation can be determined simply from Kikuchi patterns. The orientation can either be determined by indexing three independent pairs of Kikuchi lines or by comparing the observed Kikuchi pattern with an indexed Kikuchi line map. The foil orientation can be determined within an accuracy of $\pm 0.1\%$.

To determine the tilting angle in stereo experiments, the displacement of Kikuchi lines may also be used. If the specimen is tilted by an angle normal to the incident beam, the whole Kikuchi pattern shifts by a vector perpendicular to the tilting axis. From the shifting, the tilting angle may be determined within an accuracy of $\pm 0.2^\circ$.

6.3. Evaluation of Stereo Micrographs

Stereo pairs are obtained by producing two micrographs with different orientations of the specimen relative to the electron beam. If the distance of two points on the micrographs changes by the parallax p from one micrograph to another, the relative difference in height h of the two points inside the specimen is calculated from the simple parallax equation

$$h = \frac{p}{2 M \sin \theta}$$

where M is the overall magnification of the micrographs, and 2θ is the total tilting angle.

This equation is, as shown by Nankivell,⁴⁶ only correct under certain conditions, which often cannot be attained experimentally. Therefore, corrections must be added to the simple parallax equation. The most important is the correction of the tilt error. If the optical axis and the tilt axis

do not intersect (see Fig. 13), the correction term, which has to be added to Eq. (15), is

$$(\Delta h)_t = \frac{\Delta s(s_a + 2s + \Delta s) \cos \theta}{\ell_o} \quad (16)$$

The distance between the first principal plane of the objective lens and the plane that is normal to the optical axis and contains the tilt axis is ℓ_o ; this distance is approximately the focal length of the objective lens of the microscope.

This error can be kept small if Δs is small.* However, for certain

* Δs is the distance of the projection of the two points, for which the height difference has to be determined, onto the image plane.

experiments, Δs has a large value, and in this case the correction described through Eq. (16) is significant and must be taken into account.

The length s_a in Eq.(16) can be determined from

$$s_a = \Delta h_s \cdot \text{ctg } \theta,$$

where Δh_s is the change in the distance between the specimen and the first principal plane of the objective lens during the tilting experiment. This change is actually the change in the focal distance of the objective lens for the two micrographs of the stereo pairs. A calibration of the focal length ℓ' (Fig. 3) versus the "strength" of the objective lens yields Δh_s . The "strength" is represented best by the electrical current through the coils of the objective lens.

7. EXPERIMENTAL RESULTS

7.1 Experimental Results on Small Defect Clusters

The experimental results of the study on small defects in neutron-, ion-, and electron-bombarded materials have been summarized.^{5,6} Since these papers were published, it has been well established that reliable experimental results for both defect size distribution,^{5,6} and the type of small defect clusters observed in neutron-irradiated face-centered-cubic^{57,58} materials can be obtained.

In body-centered-cubic materials, the type and size distribution of the defects depend sensitively on the impurity content of the material. This was demonstrated for molybdenum in the extended studies by Eyre et al.⁵⁹⁻⁶² For niobium, Loomis⁶³ showed that the defect structure depends strongly on the amount of oxygen that is in solution in the material.

The fine structure of the small defect clusters can be studied by the "weak-beam" method. In this technique one images the defects with a weakly excited beam, i.e., a dark-field beam with a high excitation error w . On weak-beam micrographs, the defects appear as bright spots on a dark background. In this imaging technique, the resolution of details of the defects essentially improved compared with the regular bright- and dark-field images since the effective extinction length is much smaller in the weak-beam micrograph.^{8,9}

In Fig. 14, the advantage of the weak-beam micrograph is demonstrated. Figures 14(a) and (b) represent a bright-field and a dark-field micrograph, respectively, of a foil of high-purity niobium irradiated with 4×10^{19} n/cm² ($E_n > 0.1$ MeV).⁶³

The observable large defects (diameters smaller than 400 \AA) show a jerky structure in the regular bright-field and dark-field micrographs. If one images under weak-beam dark-field conditions (Fig. 14d), one finds that each defect is composed of very small clusters. The diameters of the very small clusters is just above the resolution limit of the electron microscope. However, contrast experiments by Cockayne⁶ and by Häusserman⁶⁴ indicate that in the case of heavy-ion bombarded copper foils one small defect cluster can yield more than one white spot under weak-beam conditions. The number of observable spots in Figure 14(d) is not necessarily identical with the number of defects. Further theoretical and experimental work is necessary for a full evaluation of the weak-beam micrographs.

7.2. Experimental Results on the Contrast of Small Bubbles

The dependence of the contrast behavior of the small bubbles on the focusing and imaging conditions was studied and the results of the observations were compared with the results of the "out-of-focus" contrast calculations. For this purpose, epitaxially grown gold single crystals ($\sim 600 \text{ \AA}$ to 1000 \AA thick) were irradiated with He^+ ions at energies between 25 and 150 keV and at temperatures between room temperature and 400°C . After an irradiation with $6 \times 10^{17} \text{ He}^+$ particles/cm² at temperature above 100°C , gas-filled bubbles were formed.*

*Details on the results of the irradiation experiments and the dependence of the observable defect structure (black spots or bubbles) on the irradiation conditions are described elsewhere.⁶⁵

The irradiated foils were investigated with a Siemens electron microscope operated at 100 kV.

The small bubbles (diameter smaller than $\sim 30 \text{ \AA}$) were only observable if one images the foil out of focus (see Fig. 15). The sign, size, and magnitude of the contrast depend strongly on the defocusing conditions, i.e., on the sign and distance ζ between the lower surface of the foil and the focal plane of the objective lens (compare with Fig. 6).

For a quantitative comparison of the theoretically predicted "out-of-focus" contrast (see Section 3) and the experiments, the distance ζ between the exit surface of the film and the focal plane must be known.

We determined ζ by measuring a part of the current I_{ob} through the objective lens in the different focusing conditions. The change of I_{ob} was calibrated versus the change in the distance of the focal plane, and it was found that a change of $\Delta I_{ob} = 1 \text{ \mu A}$ corresponds to a change of $\Delta \zeta = 0.0105 \text{ \mu m}$. The relation between ΔI_{ob} and $\Delta \zeta$ was linear in the distance range of interest.

The bubbles were imaged under different focusing conditions; one example of the "through the focus" series are shown in Fig. 15. If ζ is negative, the bubbles show, as predicted by the theory (Section 3.2) a contrast that has a white inner part surrounded by a weak dark ring. For positive ζ , the contrast has a black dot surrounded by a weak white ring. Figure 15 also indicates that the bubbles are invisible under "in-focus" conditions ($\zeta = 0$).

The size of the black ($\zeta > 0$) and white ($\zeta < 0$) central portion of the contrast of the small bubbles is almost independent of the exact imaging conditions and of the exact value of ζ , for distances of ζ that are not too large. However, the outer diameter of the first Fresnel fringe depends strongly on ζ .

The actual bubble size can be determined from the diameter of the central portion of the contrast. Normally, the diameter of the outer diameter is at least 50% larger than the actual bubble size. The experimental results are in good agreement with the contrast calculations described in Section 3.2. More results, especially the dependence of the contrast on the imaging condition, will be published elsewhere.

The out-of-focus contrast of bubbles with different geometrical shapes can be more complicated. Figure 6 shows the through-the-focus series of voids produced in stainless steel after irradiation with Ni^+ ions at high temperature.⁶⁶ The contrast is more complicated for $\zeta < 0$. The white center containing a black spot is surrounded by a black ring. For $\zeta > 0$ the opposite is true. Preliminary contrast calculations show that the actual size of these voids coincides with the mean diameter of the bright portion for $\zeta < 0$.

8. CONCLUSIONS

The electron microscopy contrast of defects observable in irradiated material was discussed, and emphasis was placed on the contrast of voids and bubbles. It was shown that voids and bubbles produce a phase shift of the electron wave inside the crystal. The phase difference relative to the perfect crystal can only be made visible (especially for small voids) by working out of focus.

The following important contrast features were calculated and also determined experimentally:

- A. Small voids and bubbles are only observable if the defects are imaged out of focus.

- B. The sign of the contrast depends on the sign of the defocusing conditions. To distinguish between voids and defects of other shapes, a "through-the-focus" series is required.
- C. The diameter of the inner contrast ring corresponds to the actual diameter of the bubbles in the size range between 20 Å and 80 Å.
- D. For larger bubbles, the width and intensity of the out-of-focus contrast depends on the actual size of the bubble and the thickness of the film.

9. ACKNOWLEDGMENTS

I wish to thank Drs. K. L. Merkle and M. Wilkens for many helpful and fruitful discussions. The experimental assistance of L. R. Singer and J. R. Wrobel is acknowledged. I want to thank S. G. McDonald and Dr. A. Taylor for providing their unpublished results represented in Fig. 16, Dr. B. L. Loomis for supplying the niobium specimens, and Mrs. Vera Heitsch, who patiently and efficiently typed several editions of the paper.

REFERENCES

1. Silcox, J. and Hirsch, P. B., Phil. Mag., 4: 1356 (1959).
2. Makin, M. J., Whapham, A. D. and Minter, F. J., Phil. Mag., 6: 465 (1961).
3. Hirsch, P. B., Howie, A., Nicholson, R. B., Pashley, D. W. and Whelan, M. J., Electron Microscopy of Thin Crystals, Butterworths, London, (1965).
4. Amelinckx, S., Gevers, R., Remaut, G. and Van Landyt, I. (editors), Modern Diffraction and Imaging Techniques in Materials Science, North Holland Publishing Company, Amsterdam (1970).
5. Rühle, M., Study of Small Defect Clusters in Irradiated Materials by Means of Transmission Electron Microscopy, in Symposium Proceedings: Vienna, Vol. I, pp. 113, Radiation Damage in Reactor Materials, IAEA, Vienna (1969).
6. Wilkens, M., Studies of Point Defect Clusters by Transmission Electron Microscopy, in Conference Proceedings KFA Jülich 1968; pp. 485; Seeger, A., Schumacher, D., Schilling, W. and Diehl, J., (editors), Vacancies and Interstitials in Metals, North Holland Publishing Company, Amsterdam (1970).
7. Wilkens, M., Identification of Small Defect Clusters in Particle-Irradiated Crystals by Means of Transmission Electron Microscopy, in Ref. 4, p. 233.
8. Cockayne, D. J. H., D. Phil. Thesis, University of Oxford (1970) unpublished.
9. Cockayne, D. J. H., Ray, I. L. F. and Whelan, M. J., Phil. Mag. 20: 1265 (1969).
0. Howie, A. and Whelan, M. J., Proc. Roy. Soc., A 263: 217 (1961); A 267: 206 (1962).
1. Hirsch, P.B., Howie, A. and Whelan, M.J., Phil. Trans. Roy. Soc. (London), A 252: 499 (1960).
2. Jouffrey, B. and Taupin, D., Phil. Mag. 16: 703 (1967).
3. Howie, A. and Basinski, Z. S., Phil. Mag. 17: 1039 (1968).

References (cont'd.)

14. Colliex, C., Jouffrey, B. and Taupin, D., Phil. Mag., 19: 673 (1969).
15. Howie, A., Sworn, C. H., Phil. Mag., 22: 861 (1970).
16. Howie, A., Proc. Roy. Soc., A 271: 268 (1963).
17. Wilkens, M., phys. stat. sol., 6: 939 (1964).
18. Wilkens, M., phys. stat. sol., 13: 529 (1966).
19. Ruf, H., Diplomarbeit TH Stuttgart (1968), unpublished.
20. Humphreys, C. J. and Hirsch, P. B., Phil. Mag., 18: 115 (1968).
21. Shuttleworth, R., Proc. Roy. Soc., A 63: 444 (1950).
22. Herring, C., Structure and Properties of Solid Surfaces (edited by Cromer, R. and Smith, C. S.) University of Chicago Press, Chicago (1953).
23. Lidiard, A. B. and Nelson, R. S., Phil. Mag., 17: 425 (1968).
24. Nolfi, F. W., Jr. and Johnson, C. A., to be published.
25. Ashby, M. F. and Brown, L. M., Phil. Mag., 8: 1649 (1963).
26. Van Landuyt, J., Gevers, R. and Amelinckx, S., phys. stat. sol., 10: 319 (1965).
27. Ingram, J., J. Appl. Phys., 40: 5030 (1969).
28. Ruedl, E. and Staroste, E., Proc. VIIieme Congress International de Microscopie Electronique, Grenoble (1970), Vol. I, p. 343.
29. Ruedl, E., in: Irradiation Effects on Structural Alloys for Nuclear Reactor Applications, ASTM STP 484, American Society for Testing and Materials, 1970, pp. 300.
30. Gevers, R., phys. stat. sol., 9: 135 (1965).
31. Amelinckx, S., The Study of Planar Interfaces by Means of Electron Microscopy, in Ref. 4, p. 257.
32. Rühle, M. and Wilkens, M., to be published.
33. Born, M. and Wolf, E., Principles of Optics, Pergamon Press, Oxford-London, New York (1970).

References (cont'd.)

34. Wilkens, M., private communication.
35. Love, A.E.H., A Treatise of the Mathematical Theory of Elasticity, University Press, Cambridge (1952).
36. Rühle, M. and Wilkens, M., to be published.
37. Rühle, M. and Wilkens, M., to be published.
38. Rühle, M. and Wilkens, M., Proc.VII-ieme Congress International de Microscopie Electronique, Grenoble (1970), Vol. I, pp. 311.
39. Maher, D. M., Perrin, R. C. and Bullough, R., phys. stat. sol., 43: 707 (1970).
40. Rühle, M., to be published.
41. McIntyre, K. G. and Brown, L. M., J. Phys. Radium, 27-C3: 178 (1966).
42. Brown, L. M. and Mazey, D. J., Phil. Mag., 10: 1081 (1964).
43. Chik, K. P., Wilkens, M. and Rühle, M., phys. stat. sol., 23: 113 (1967).
44. Ashby, M. F. and Brown, L. M., Phil. Mag., 8: 1083 (1963).
45. Diepers, H. and Diehl, J., phys. stat. sol., 16: k109 (1966).
46. Nankivell, J. F., Optik, 20: 171 (1963).
47. Groves, G. and Kelly, A., Phil. Mag., 6: 1527 (1961); 7: 892 (1962).
48. Edmunson, B. and Williamson, G. K., Phil. Mag., 9: 277 (1964).
49. Amelinckx, S., in: The Interaction of Radiation with Solids, North Holland Amsterdam (1964) pp. 682.
50. Ruedl, E. and Amelinckx, S., J. Phys. Soc. Jap., 18-Suppl.III: 195 (1963).
51. Maher, D. M. and Eyre, B. L., Phil. Mag., 23: 409 (1971).
52. Maher, D. M. and Eyre, B. L., in: Proc. 4th European Reg. Conf. on Electron Microscopy, Vol. I, Rome (1968) pp. 373.
53. Silcock, J. M. and Tunstall, W. J., Phil. Mag., 10: 361 (1964).

References (cont'd.)

54. Mazey, D. J., J. Nucl. Mat., 35: 60 (1970).
55. Thomas, G., Kikuchi Electron Diffraction and Application, in Ref. 4, p. 159.
56. Rühle, M. and Crump III, J. C., phys. stat. sol. (a), 2: 257 (1970).
57. Rühle, M. Häussermann, F. and Rapp, M., phys. stat. sol. 39: 609 (1970).
58. Rühle, M., Häussermann, F. and Rapp, M., phys. stat. sol. 39: 621 (1970).
59. Eyre, B. L., Maher, D. M. and Bartlett, A. F., Phil. Mag., 23: 439 (1971).
60. Maher, D. M., Loretto, M. H. and Bartlett, A. F., AERE Report R 6518.
61. Maher, D. M., Eyre, B. L. and Bartlett, A. F., AERE Report R6614.
62. Eyre, B. L. and Maher, D. M., AERE Report R 6618.
63. Loomis, B. A., private communication.
64. Häussermann, F., Proc. VII-ieme Congress International de Microscopie Electronique, Grenoble (1970), Vol. I, pp. 301.
65. Merkle, K. L. and Rühle, M., to be published.
66. McDonald, S. D. and Taylor, A., to be published.

FIGURE CAPTIONS

Fig. 1. Schematic representation illustrating the notation used. The case of a "penny-shaped" bubble is considered. A bubble with arbitrary shape must be decomposed in a sequence of bubbles as shown in this figure. The foil thickness is t , subdivided in the thickness of the bubble z_2 and in the thicknesses z_1 and z_3 of the parts above and below the bubble (perfect crystal). The wave vector of the incoming and reflected beams are k_o and k_g , respectively.

Fig. 2. Intensity thickness relationship for $w = 0$ (bright field I_T and dark field I_S). Normal and anormal absorption are taken into account. The value of the anomalous absorption coefficient was $\kappa = 0.1$; the values of the normal absorption coefficients are noted in the diagram.

Fig. 3. Dependence of contrast for bright field (C_T) and dark field (C_S) from the foil thickness. The thickness of the "penny-shaped" bubble is $0.1\xi_g$, the normal absorption factor μ is $\mu = \frac{1}{\xi_g}$; $w = 0$.

Fig. 4. Variation of bright field (C_T) and dark field (C_S) contrast with increasing bubble thickness: $z_2/\xi_g = R_o/\xi_g$. The thickness of the foil is $4 \xi_g$. The different normal absorption factors μ are noted; $w = 0$.

Fig. 5. Contrast of spherical bubbles of two different sizes. Bright field images. The change in the normalized intensity I/I_0 (I_0 = background intensity) is plotted over the reduced bubble radius $\rho = r/R_b$; R_b = bubble radius; contrast $C_I = I/I_0 - 1$; $w = 0$.

Fig. 6. Schematic representation illustrating the notation used for "out-of-focus" calculations. The center of the bubble lies at $x = y = \xi = \eta = 0$. ξ_1 describes the distance between the lower foil surface and the image plane.

Fig. 7. Results of "out-of-focus" calculations (mean inner potential $V_0 = -10V$); I/I_0 (I_0 = background intensity) is plotted over the reduced radius of the defect $\rho = r/r_0$ (r_0 = radius of the defect) for different values of $\beta = \pi k_0 r_0^2 / \zeta$. Note that the "out-of-focus" contrast extends over the actual size of the defect. k_0 = wave vector of the electrons, ζ = defocusing distance. a) spheres; b) cylindrical disks. The thickness of the disks is equal to r_0 . ($w = 0$)

Fig. 8. Contrast width of the inner (d_{in}/d_b) and outer (d_{out}/d_b) reduced diameter of the first dark Fresnel fringe as a function of the actual bubble diameter (defocusing distance $\zeta = -8000 \text{ \AA}$).
 d_b = diameter of the spherical bubble.

Fig. 9. "Out-of-focus" contrast calculations for large bubbles ($R_b = 0.4 \xi_g$, $\xi_g = 250 \text{ \AA}$). The foil thickness is $3.75 \xi_g$ for $\zeta = +6000 \text{ \AA}$ and $\zeta = -6000 \text{ \AA}$. The reduced intensity I/I_0 ($I_0 =$ background intensity) is plotted versus $\rho = r/R_b$. The "in-focus" contrast ($w = 0$) is also represented.

Fig. 10. Black-white contrasts (BW contrasts) in a He^+ -bombarded gold film. The diffraction vector $\vec{g} = (220)$ is noted, foil orientation $[001]$, dark-field picture.

Fig. 11. Schematic plot of the depth oscillations of the BW-contrast from small defects (Frank dislocation loops, small voids) of vacancy type. The calculated contrast figures are drawn at that depth position at which the loop centers were assumed. d.f. = dark field, b. f. = bright field. g = diffraction vector, b = Burgers vector (in the case of Frank loops only). For defects of interstitial type, the black and white contrast portions must be interchanged. In the intermediate (transition) regions $I_{k,k+1}$ complicated contrast figures are calculated.

Fig. 12. Type of contrasts of spherical voids (inclusions) as a function of the reduced radius R_v/ξ_g ($R_v =$ radius of the void, $\xi_g =$ extinction length) and of the normalized misfit parameter P .
Region A: Black-white contrasts with depth oscillations; Region B: black-white contrasts without depth oscillations; Region C: no black-white contrasts calculated, pure thickness contrast.

- Fig. 13. Positions of the specimen for stereo pairs. s_a = distance between tilt axis and optical axis, Δh : height difference of two points inside the foil. Tilt angle $2\theta = \theta_+ + \theta_-$.
- Fig. 14. Defects in neutron-irradiated niobium (oxygen content < 0.02 wt. %, neutron dose 4.10^{19} n/cm², $E_n > 0.1$ MeV), foil orientation near [110]. The diffraction vector $g = (\bar{1}\bar{1}2)$ is noted. a) bright-field image; b) dark-field image (w slightly positive); c) $w \sim 0.5$; d) weak-beam picture. In the weak beam dark field a high density of small defects are resolved.
- Fig. 15. Au-film irradiated with 6×10^{16} He⁺/cm² at 100°C. Through-the-focus series. The differences in $\zeta = \Delta f$ are noted. The contrast of the center changes from dark (with white Fresnel ring) to bright (with dark Fresnel ring). Foil orientation (001), g close to (200).
- Fig. 16. Voids in stainless steel irradiated with 3 MeV Ni⁺ ions.⁶⁶ Through-the-focus series. The change in ζ from micrograph to micrograph (left to right) is ~ 3000 Å. The contrast reverses from underfocused to overfocused; the voids are invisible under "in-focus" conditions.

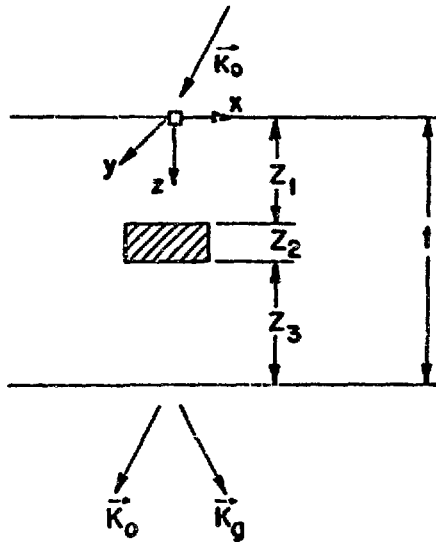


Fig. 1. Schematic representation illustrating the notation used. The case of a "penny-shaped" bubble is considered. A bubble with arbitrary shape must be decomposed in a sequence of bubbles as shown in this figure. The foil thickness is t , subdivided in the thickness of the bubble z_2 and in the thicknesses z_1 and z_3 of the parts above and below the bubble (perfect crystal). The wave vector of the incoming and reflected beams are k_0 and k_g , respectively.

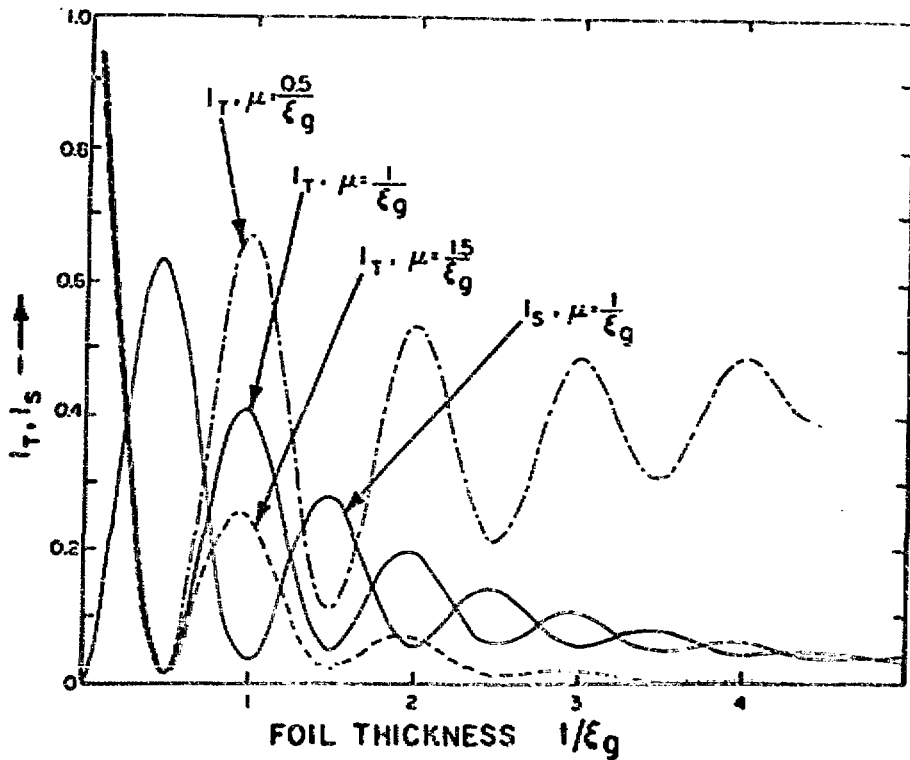


Fig. 2. Intensity thickness relationship for $w = 0$ (bright field I_T and dark field I_S). Normal and anomalous absorption are taken into account. The value of the anomalous absorption coefficient was $\kappa = 0.1$; the values of the normal absorption coefficients are noted in the diagram.

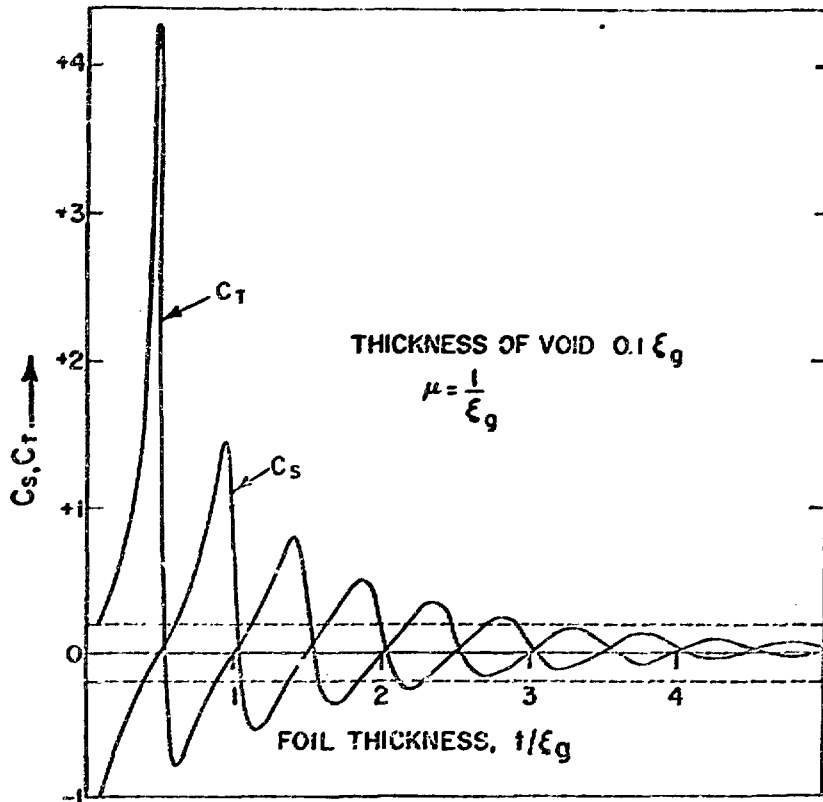


Fig. 3. Dependence of contrast for bright field (C_T) and dark field (C_S) from the foil thickness. The thickness of the "penny-shaped" bubble is $0.1\xi_g$, the normal absorption factor μ is $\mu = \frac{1}{\xi_g}$; $w = 0$.

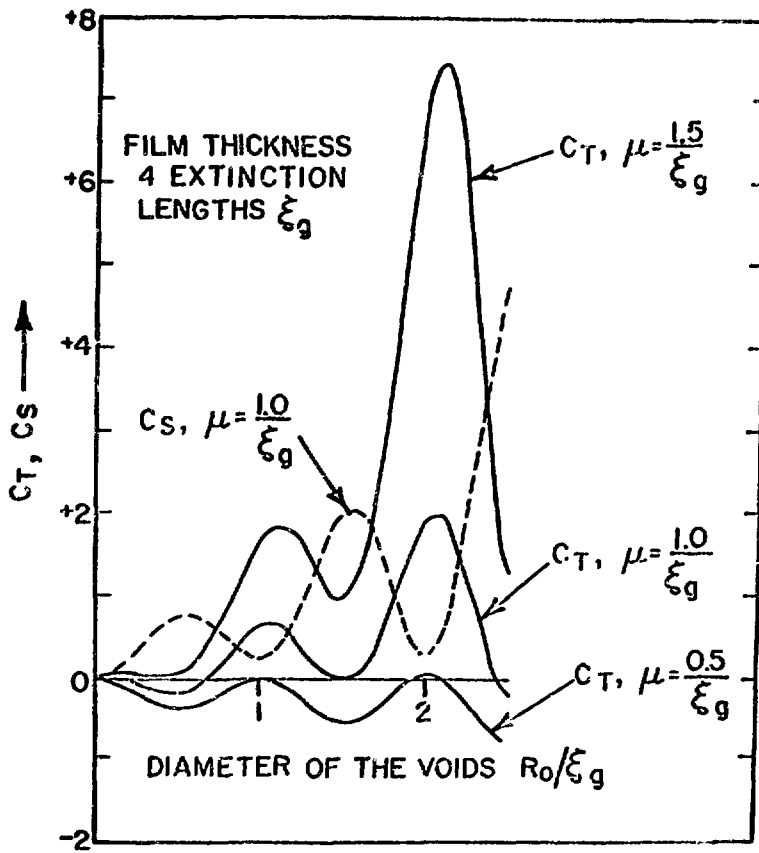


Fig. 4. Variation of bright field (C_T) and dark field (C_S) contrast with increasing bubble thickness $z_2/\xi_g = R_0/\xi_g$. The thickness of the foil is $4 \xi_g$. The different normal absorption factors μ are noted; $w = 0$.

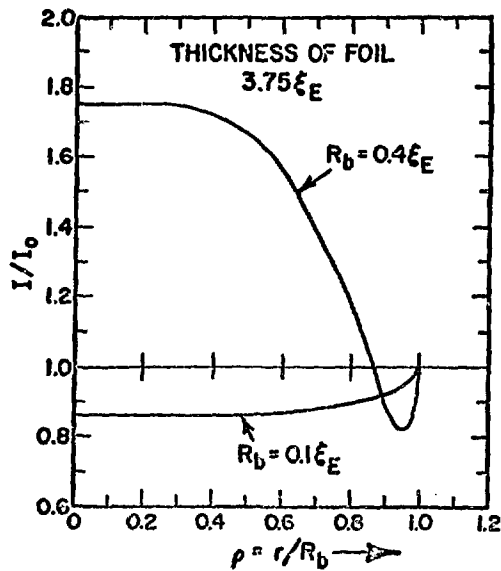


Fig. 5. Contrast of spherical bubbles of two different sizes. Bright field images. The change in the normalized intensity I/I_0 (I_0 = background intensity) is plotted over the reduced bubble radius $\rho = r/R_b$; R_b = bubble radius; contrast $C_T = I/I_0 - 1$; $w = 0$.

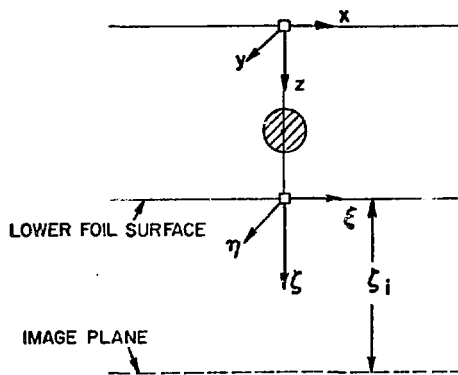


Fig. 6. Schematic representation illustrating the notation used for "out-of-focus" calculations. The center of the bubble lies at $x = y = \xi = \eta = 0$. ξ_i describes the distance between the lower foil surface and the image plane.

Fig. 7a

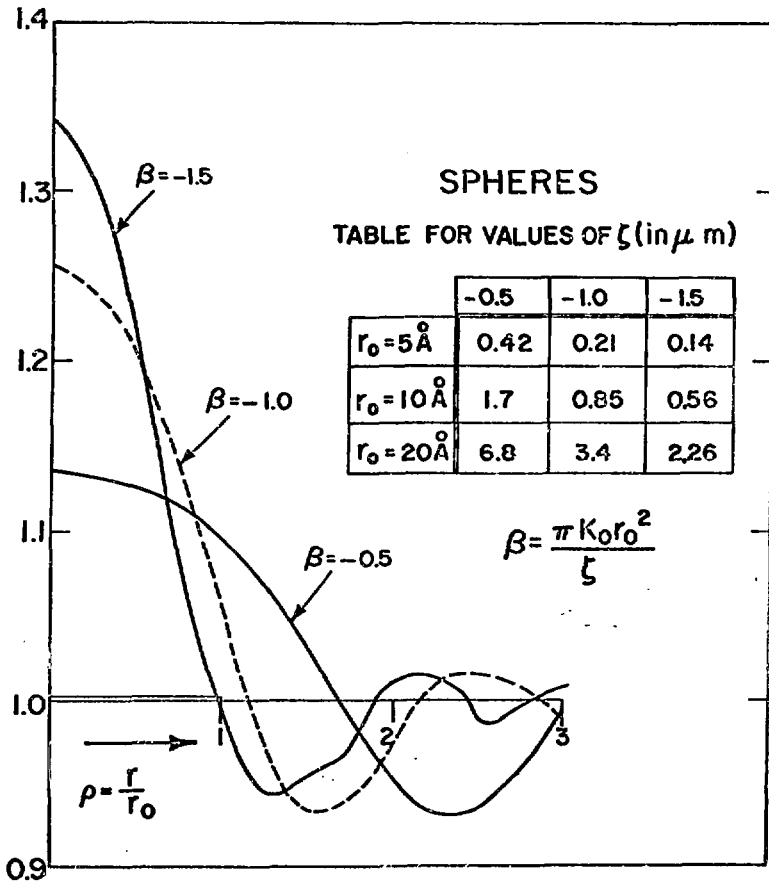


Fig. 7. Results of "out-of-focus" calculations (mean inner potential $V_0 = -10\text{V}$); $1/I_0$ (I_0 = background intensity) is plotted over the reduced radius of the defect $\rho = r/r_0$ (r_0 = radius of the defect) for different values of $\beta = \pi k_0 r_0^2 / \zeta$. Note that the "out-of-focus" contrast extends over the actual size of the defect. k_0 = wave vector of the electrons, ζ = defocusing distance. a) spheres; b) cylindrical disks. The thickness of the disks is equal to r_0 . ($w = 0$)

Fig. 7b

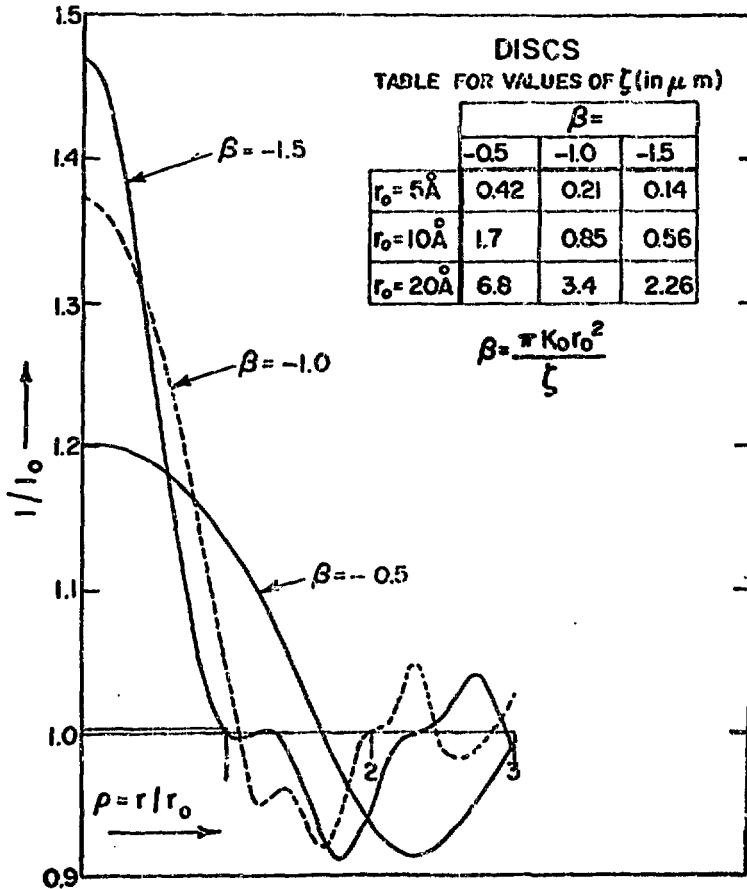


Fig. 7. Results of "out-of-focus" calculations (mean inner potential $V_0 = -10\text{V}$); I/I_0 ($I_0 =$ background intensity) is plotted over the reduced radius of the defect $\rho = r/r_0$ ($r_0 =$ radius of the defect) for different values of $\beta = \pi k_0 r_0^2 / \zeta$. Note that the "out-of-focus" contrast extends over the actual size of the defect. $k_0 =$ wave vector of the electrons, $\zeta =$ defocusing distance. a) spheres; b) cylindrical disks. The thickness of the disks is equal to r_0 . ($w = 0$)

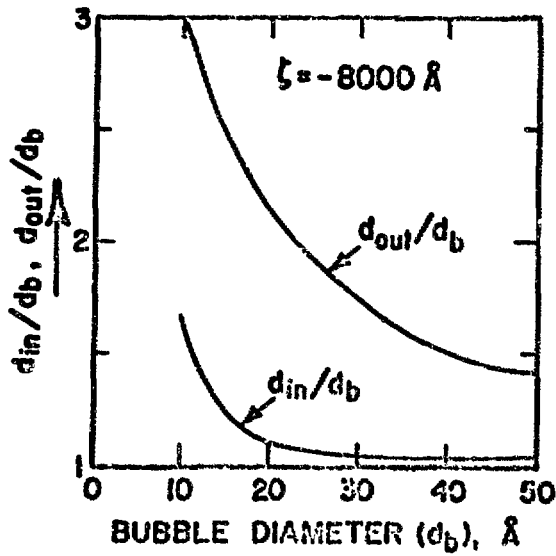


Fig. 8. Contrast width of the inner (d_{in}/d_b) and outer (d_{out}/d_b) reduced diameter of the first dark Fresnel fringe as a function of the actual bubble diameter (defocusing distance $\zeta = -8000 \text{ \AA}$).
 d_b = diameter of the spherical bubble.

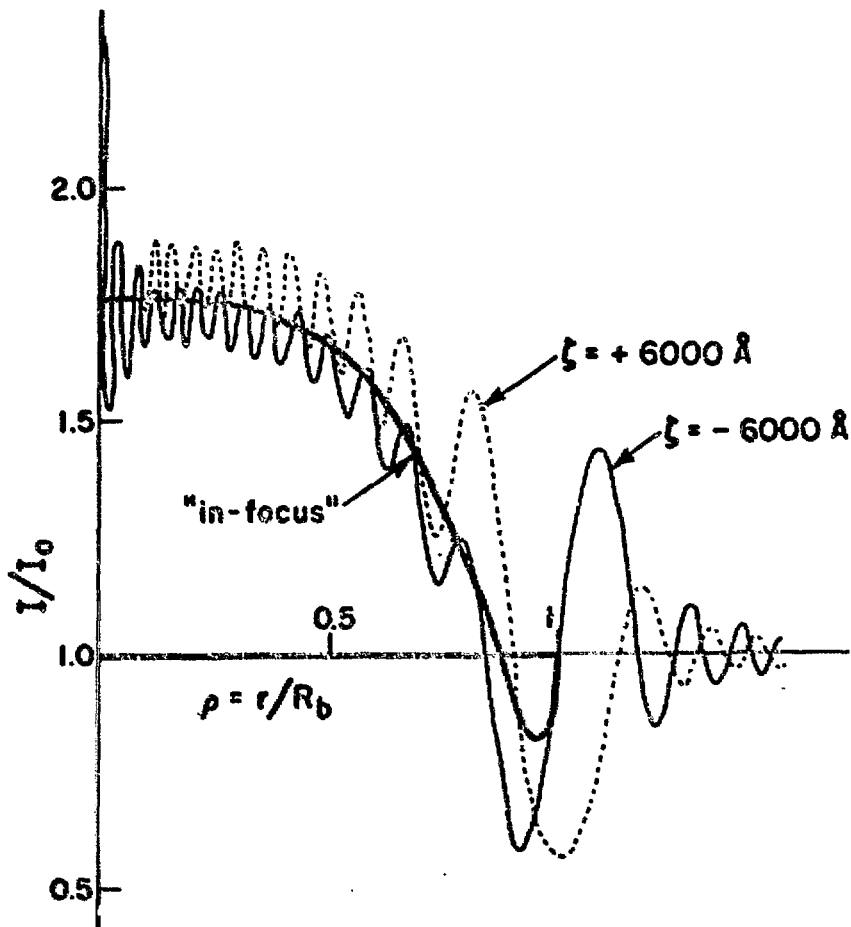


Fig. 9. "Out-of-focus" contrast calculations for large bubbles ($R_b = 0.4\xi_g$, $\xi_g = 250 \text{ \AA}$). The foil thickness is $3.75\xi_g$ for $\zeta = +6000 \text{ \AA}$ and $\zeta = -6000 \text{ \AA}$. The reduced intensity I/I_0 (I_0 background intensity) is plotted versus $\rho = r/R_b$. The "in-focus" contrast ($w = 0$) is also represented.

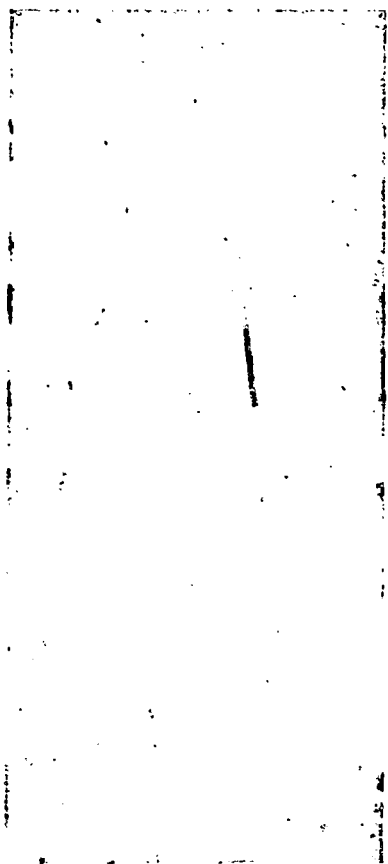


Fig. 10. Black-white contrasts (EW contrasts) in a He^+ -bombed gold film. The diffraction vector $\vec{g} = (220)$ is noted, foil orientation $[001]$, dark-field picture.

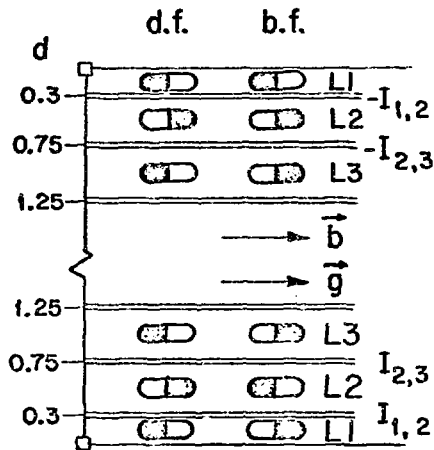


Fig. 11. Schematic plot of the depth oscillations of the BW-contrast from small defects (Frank dislocation loops, small voids) of vacancy type. The calculated contrast figures are drawn at that depth position at which the loop centers were assumed. d.f. = dark field, b. f. = bright field. g = diffraction vector, b = Burgers vector (in the case of Frank loops only). For defects of interstitial type, the black and white contrast portions must be interchanged. In the intermediate (transition) regions $I_{k,k+1}$ complicated contrast figures are calculated.

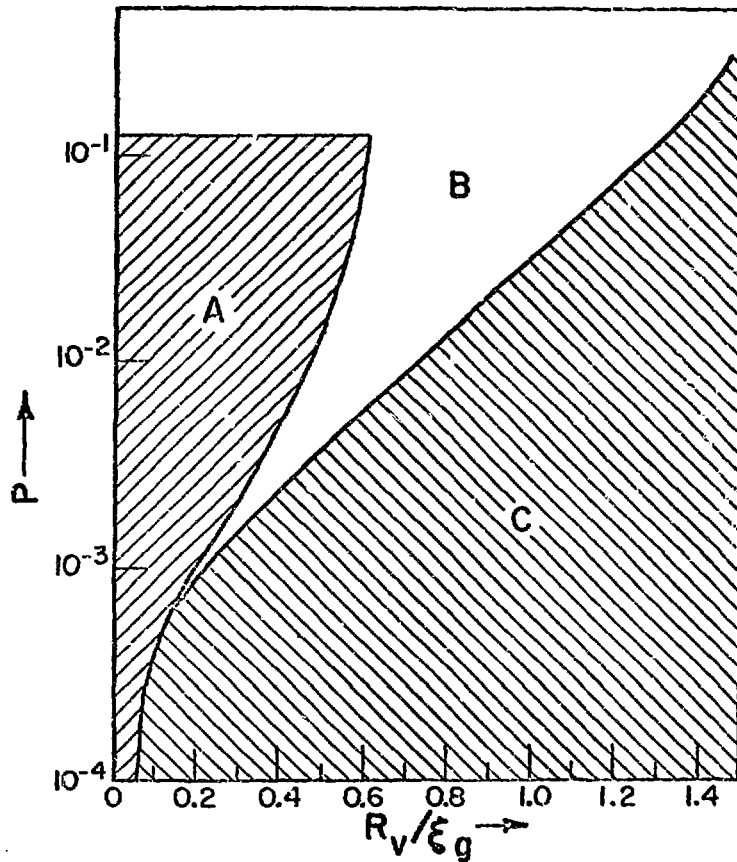


Fig. 12. Type of contrasts of spherical voids (inclusions) as a function of the reduced radius R_v/ξ_g (R_v = radius of the void, ξ_g = extinction length) and of the normalized misfit parameter P .

Region A: Black-white contrasts with depth oscillations; Region B: black-white contrasts without depth oscillations; Region C: no black-white contrasts calculated, pure thickness contrast.

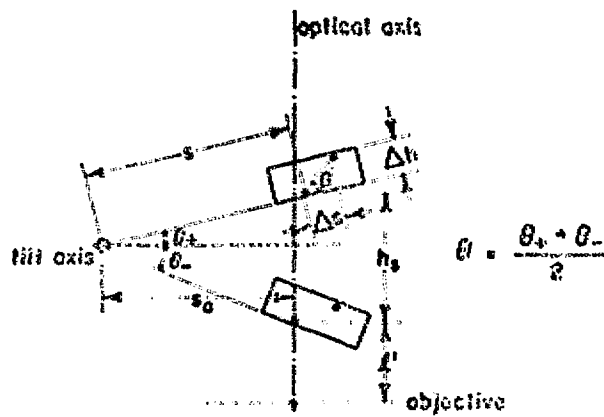
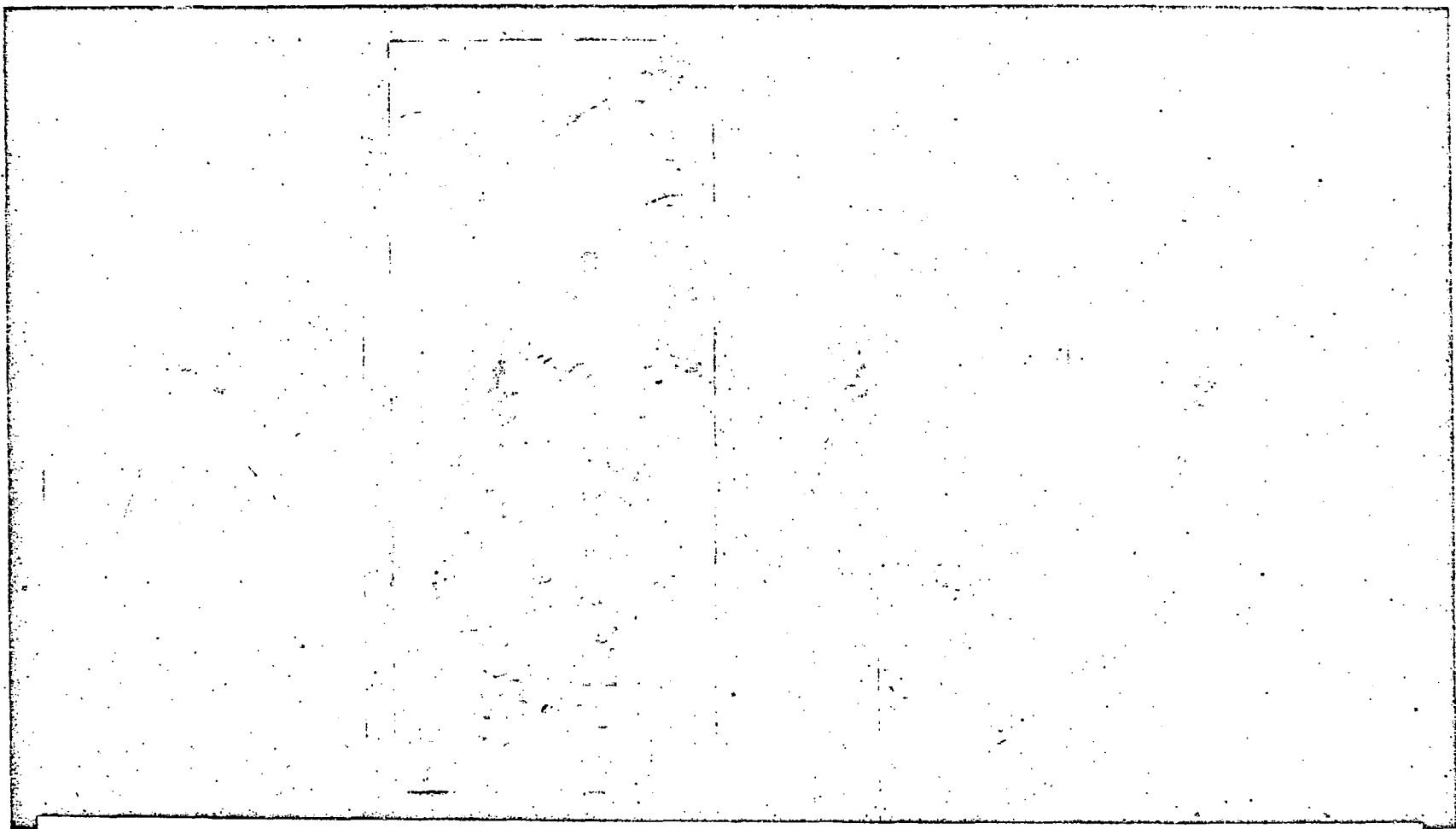


Fig. 13. Positions of the specimen for stereo pairs. s_0 = distance between tilt axes and optical axis, Δh : height difference of two points inside the foal. Tilt angle $\theta = \frac{\theta_+ + \theta_-}{2}$.



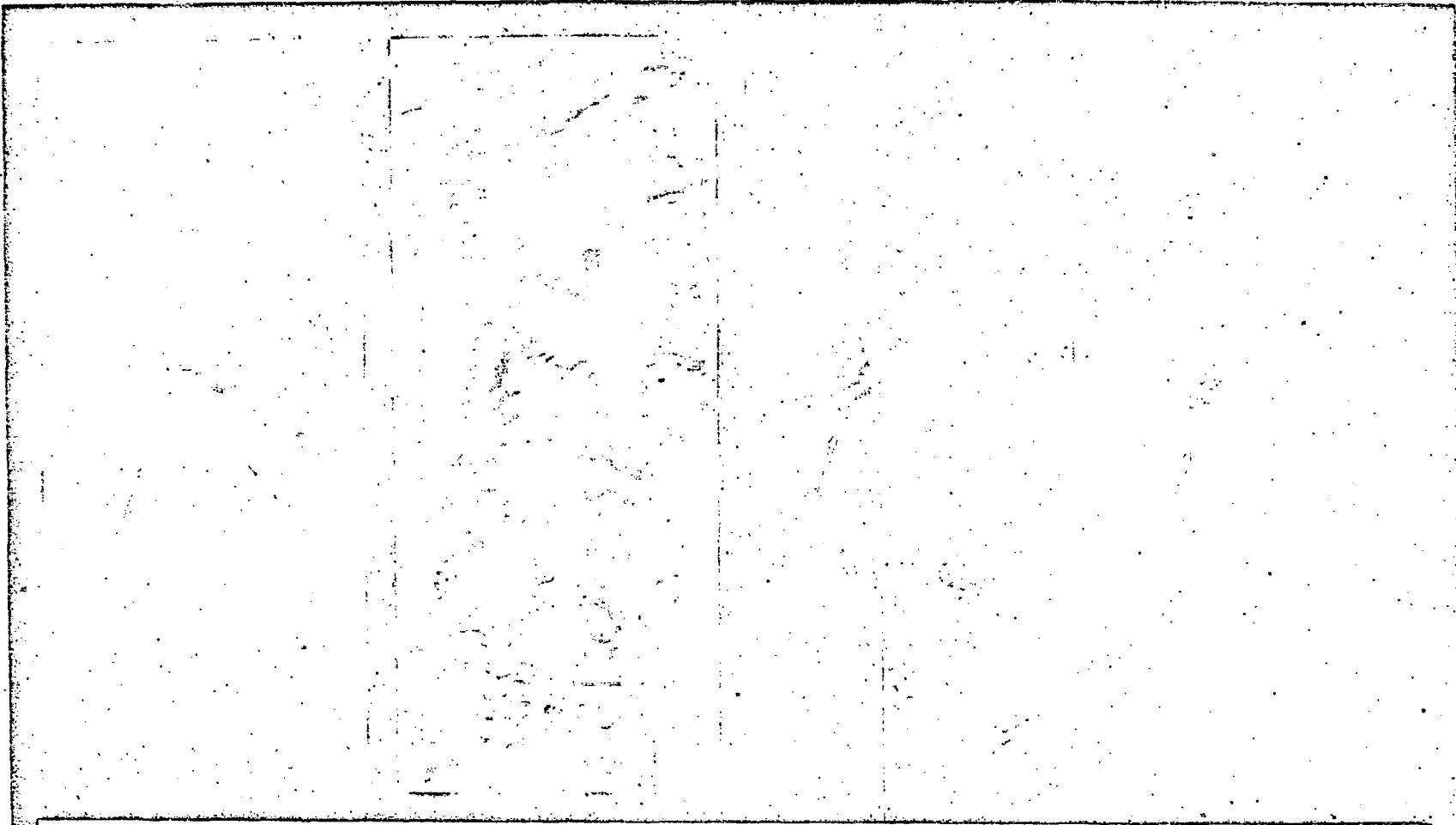
(a)

(b)

(c)

(d)

Fig. 14. Defects in neutron-irradiated niobium (oxygen content < 0.02 wt. %, neutron dose $4 \cdot 10^{19}$ n/cm², $E_n > 0.1$ MeV), foil orientation near [110]. The diffraction vector $g = (1\bar{1}2)$ is noted. a) bright-field image; b) dark-field image (w slightly positive); c) $w = 0.5$; d) weak beam picture. In the weak beam dark field a high density of



(a) (b) (c) (d)

Fig. 14. Defects in neutron-irradiated niobium (oxygen content < 0.02 wt. %, neutron dose $4 \cdot 10^{19}$ n/cm², $E_n > 0.1$ MeV), foil orientation near [110]. The diffraction vector $g = (\bar{1}\bar{1}2)$ is noted. a) bright-field image; b) dark-field image (w slightly positive); c) $w \sim 0.5$; d) weak-beam picture. In the weak beam dark field a high density of small defects are resolved.

2

10

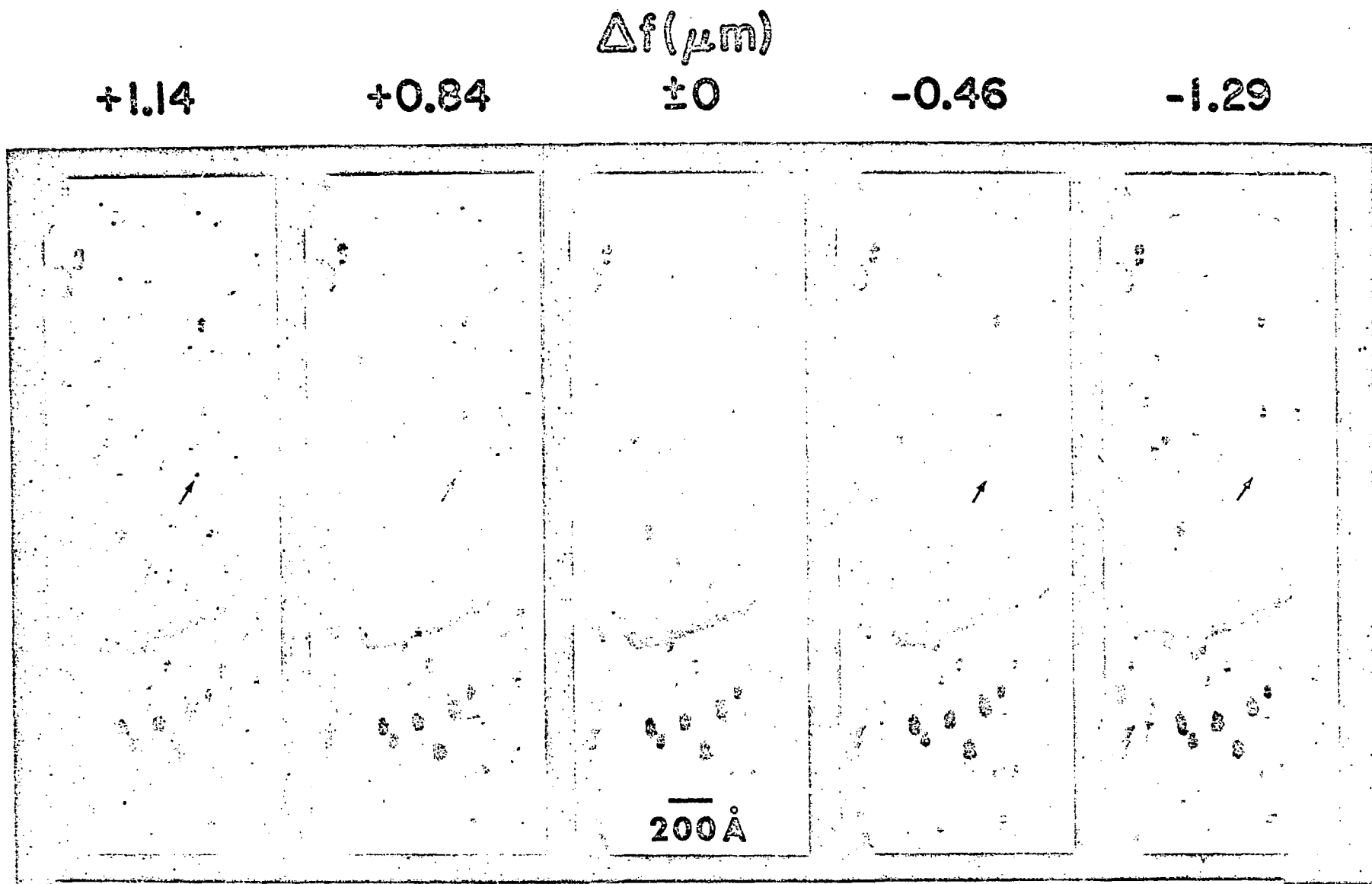


Fig. 15. Au-film irradiated with $6 \times 10^{16} \text{ He}^+/\text{cm}^2$ at 100°C . Through-the-focus series. The differences in $\zeta = \Delta f$ are noted. The contrast of the center changes from dark (with white Fresnel ring) to bright (with dark Fresnel ring). Foil orientation (001), g close to (200).

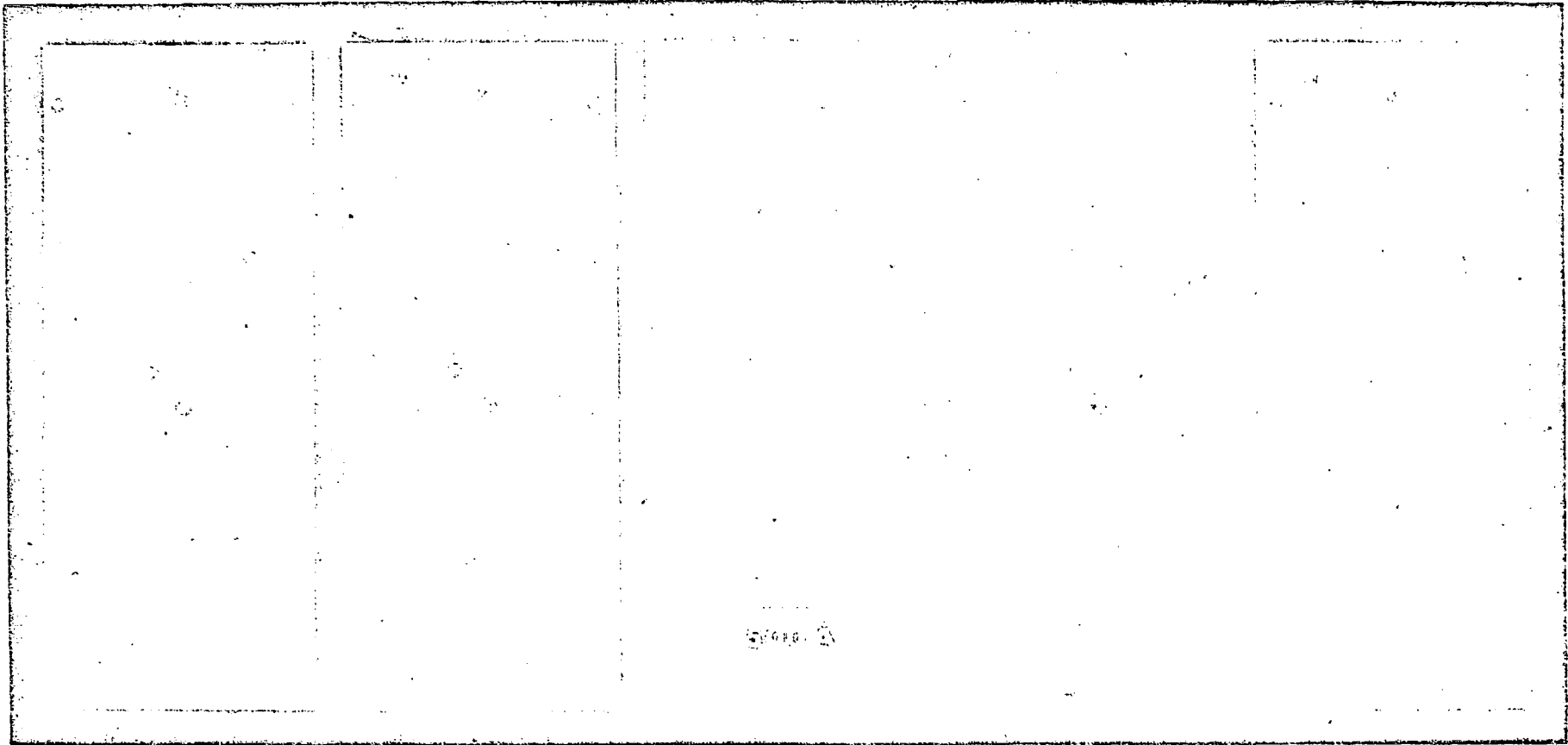


Fig. 16. Voids in stainless steel irradiated with 3 MeV Ni⁺ ions.⁶⁶ Through-the-focus series. The change in ζ from micrograph to micrograph (left to right) is $\sim 3000 \text{ \AA}$. The contrast reverses from underfocused to overfocused; the voids are invisible under "in-focus" conditions.